Master's Thesis

Millimeter Wave Antenna Technology in Mobile Terminal and Station

Jakob Helander

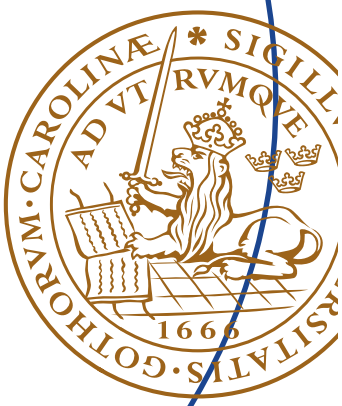

Department of Electrical and Information Technology,
Faculty of Engineering, LTH, Lund University, June 2014.

Millimeter Wave Antenna Technology in Mobile Terminal and Station

Jakob Helander
mat08jhe@student.lu.se

Department of Electrical and Information Technology
Lund University

LUND
UNIVERSITY

SONY

Supervisors:
Daniel Sjöberg, EIT
Zhinong Ying, Sony Mobile Communications

June 30, 2014

Printed in Sweden
E-huset, Lund, 2014

Acknowledgements

First and foremost I would like to thank Daniel Sjöberg and Zhinong Ying for making this thesis possible. Their expertise as supervisors and their guidance have strongly contributed to the progress of the thesis and my development as a student. I would also like to thank Mats Gustafsson and Alexander Bondarik for their professional support and inspiring discussions. They have made me feel welcome at the department and have shown great interest in my work.

In addition, a thank you directed to Thomas Bolin and Erik Bengtsson for taking part in all meetings and for giving a lot of significant input to help with my progress. I thank Casimir Ehrenborg for all discussions we have had in our common work room. We have in that sense shared the journey towards our degree in an extraordinary fashion. I am also grateful for the help I received from Carl Gustafsson. He took his time to help me with and discuss the channel model, and his expertise was greatly needed. All other members at the department also deserves a thanks, as they have greatly contributed to show the positive atmosphere that exists within the group.

I thank all my relatives for their endless encouragement of the sort that only family can contribute with. Lastly I would like to dedicate a big thanks to Luna Perschl for the help with all graphical matters, her never-ending support and her patience with me.

Abstract

In this thesis, millimeter wave (mmWave) antennas have been investigated for future cellular communication systems. For supporting high quality multimedia applications in smart phones and tablets, the wider bandwidths at mmWave frequencies can be used to increase the achievable data rates compared to today's standards. The higher operational frequency increases propagation losses, thus implementation of antenna arrays in the mobile station is a way to compensate additional losses with higher gain.

A literature study of recent advancements in mmWave technology has been carried out, to motivate a choice of antenna types for usage in mobile stations. The study points out the state of the art of the current research front regarding mmWave antennas.

Three different antennas have been selected and modeled using the simulation software CST. The target operational frequencies are set to 15 GHz and 28 GHz. The chosen designs were a patch antenna, a dielectric resonator antenna (DRA) and an open-ended substrate integrated waveguide (SIW) antenna. The designs have been evaluated and compared with respect to requirements on size, bandwidth, radiation efficiency and gain.

The single element designs of the patch and the DRA have similar characteristics with broadside radiation. The DRA achieved the highest radiation efficiency and the largest bandwidth. The SIW antenna radiates in the direction of the waveguide axis, and has the lowest radiation efficiency and the narrowest bandwidth.

4×1 and 8×1 phased arrays have been constructed using the single element designs in order to establish beamsteering. A physical channel model has been used to estimate the required minimum gain at the mobile station. The array configurations have then been evaluated in terms of the coverage efficiency of their total scan pattern. Other considered parameters are maximum gain and the mutual coupling. Moreover, subarray systems of the arrays are tried out to improve the obtained coverage efficiency. This part has illustrated the viability of evaluating the total scan pattern from phased array antennas in terms of coverage efficiency, a new characterization method for phased array systems.

The array simulations indicated that subarray systems using edge-radiating SIW arrays show good promise in achieving a large coverage. Phased arrays using patch and DRA elements can obtain large coverage in one hemisphere.

Table of Contents

Chapter 1
Introduction

1.1 Background

The new generation of wireless devices has lead to a rapid increase in total mobile data traffic. The usage of smart phones and tablets requires the support of high quality multimedia applications, and as the capacity demands will continue to increase as technology advances, the necessity of higher data rates cannot be ignored. Using more bandwidth directly translates into higher data rates, and as today's cellular bands are restricted to carrier frequencies between $\sim 800\,\text{MHz}$ and $\sim 2.6\,\text{GHz}$ where the channel bandwidths are relatively narrow ($\sim 20\,\text{MHz}$), a potential solution is to use higher frequencies where the wider bandwidths available can be exploited. Thus, for future generations of cellular communication systems, the millimeter-wave (mmWave) frequency bands ($10-70\,\text{GHz}$) have recently gained a lot of attention [1].

When moving up to higher frequencies however, new requirements are put on the antennas on the mobile- and base station. When the operational wavelength decreases, the propagation loss increases simultaneously, thus requiring that these losses need to be compensated for. Antennas with high gain, which are feasible using array configurations, can make up for these losses. Fortunately, as a general rule the antenna dimensions decrease simultaneously with operating wavelength, thus enabling this integration of arrays on a mobile platform. High-gain antennas are however highly directive, increasing the probability of the beam being interrupted. Using phased array antennas the beam can be steered to an available path by adjusting the phase input of every antenna element [2]. The high directivity also indicates the need of obtaining a large total coverage using beamsteering in order to always be able to establish a link.

The mmWave bands at $15\,\text{GHz}$ ($\lambda = 20\,\text{mm}$) and $28\,\text{GHz}$ ($\lambda = 10.7\,\text{mm}$), where channel bandwidths $> 500\,\text{MHz}$ are available, can be seen as suitable bands for cellular communication, as additional losses from precipitation (e.g., rainfall and snowfall) and atmospheric absorption can be held relatively small with today's cell sizes ($\sim 200\,\text{m}$) [1]. However, for the choice of antenna types a lot of insight can be obtained by studying the recent advancements regarding antennas for the $60\,\text{GHz}$ band. With similar preconditions, studies have been made to a wide extent within this band mainly because it is unlicensed with a large channel bandwidth ($57-66\,\text{GHz}$). The atmospheric absorption peak occuring at 60 GHz has however

limited the use of this band to short-range transmissions, such as wireless local area networks (WLAN) [3].

1.2 Course of Action and Targets

The first aspect of this thesis is finding proper antenna candidates for usage in the mobile station. A literature study done within the area of mmWave antennas can motivate what type of antennas that show good potentials for future generations of cellular communication applications. The first target is thus to:

I Select a series of antenna types to model for future simulations, based on encountered research literature. The models will be evaluated regarding radiation pattern characteristics, gain, radiation efficiency ($\geq 50\,\%$), and bandwidth ($\geq 500\,\mathrm{MHz}$). To enable mass production, the complexity of the design should be held small while realizable through low-cost fabrication processes. Moreover, their size should be small enough to make array configurations implementable on the limited area available on a cellphone.

When the antenna types and their respective design have been chosen, the next step is to model the single elements. The antennas will be designed for the 15 GHz and 28 GHz bands respectively:

II Set up models of the chosen antennas as single elements and perform simulations. The designs will be compared regarding the above mentioned parameters.

When finished designs of the single element antennas have been obtained, array configurations of these will be implemented in a phone case model. The target of evaluation of the arrays are the following:

III Set up a physical propagation model from base station to mobile terminal. The propagation model is used to find a minimum required gain for the mobile antenna.

IV With respect to this gain level, evaluate the array configurations, and subarray systems of these in terms of achievable coverage, maximum gain, mutual coupling and module sizes.

1.3 Outline of the Thesis

The outline of the thesis is constructed as follows: In Chapter 2 an introductory theory regarding antenna parameters and other necessary knowledge considering this thesis in particular is given. In Chapter 3 the study done within the area of mmWave antennas are presented, where different antenna types and their performances are summarized. Moreover, this chapter is finalized by motivating the choice of antennas for design and further evaluation from the study made. In Chapter 4 a more thorough underlying theory of the selected antennas is presented together with each respective design approach. In Chapter 5 the dimensions, results and performances of the modeled antennas are presented and compared with

one another. Then, in Chapter 6 the novel approach of evaluating phased arrays in terms of their coverage efficiency is presented. An estimated channel model is set up to describe the most possible link scenarios. In Chapter 7 the simulation results of the array configurations in a phone case are presented. Here, different sizes and combinations of the array configurations are compared relative to their performance with respect to the parameters mentioned in the previous chapter. Final conclusions are presented in Chapter 8, and suggested future work in Chapter 9.

Chapter 2

Basic Antenna Parameters

An antenna is the part of a system that receives or radiates electromagnetic (EM) waves. As a part of a transmitting system it converts electrical currents into EM waves, and as a part of a receiving system it does the exact opposite. Antennas are components that are used within many different applications, such as GPS, radars, satellites, radios, TVs and cellphones. Since the application areas are well separated regarding, e.g. transmitted data rate, power and distances between receiving and transmitting systems, a lot of different designs exists that are used within the different areas. Antenna designs usually consist of a resonant element that radiates on its resonance frequency. Antenna designs that are of special importance to this thesis will be explained in Chapter 4.

For characterization of the design of an antenna as well as its performance, there exist several parameters that need consideration. In this chapter, the most fundamental ones are introduced together with additional parameters that are of specific interest in this thesis.

2.1 Radiated Far-Fields

The far-field region is defined according to the IEEE Standard 145-1993 [4] as the region where the angular field distribution is independent of the distance from a specific point in the antenna region. From the electric- ($\boldsymbol{J}$) or magnetic ($\boldsymbol{J}_{\mathrm{m}}$) current density on the antenna element, the far-field radiation can be found through an operation similar to a Fourier transform, using the following integral over the whole volume the antenna addresses:

$$\begin{aligned} \boldsymbol{F}(\theta,\phi) &= \boldsymbol{F}(\hat{\boldsymbol{r}}) = \int \boldsymbol{J}(\boldsymbol{r}')\mathrm{e}^{\mathrm{j}k\hat{\boldsymbol{r}}\cdot\boldsymbol{r}'}\,\mathrm{d}V' \\ \hat{\boldsymbol{r}} &= \hat{\boldsymbol{x}}\cos\phi\sin\theta + \hat{\boldsymbol{y}}\sin\phi\sin\theta + \hat{\boldsymbol{z}}\cos\theta \end{aligned} \tag{2.1.1}$$

where $\boldsymbol{r}'$ denotes an arbitrary point of the antenna element, $\hat{\boldsymbol{r}}$ is the direction of radiation, k is the free space wavenumber and $\boldsymbol{F}(\theta,\phi)$ is the obtained radiation vector. Since the electric field $\boldsymbol{E}(\theta,\phi)$ and the magnetic field $\boldsymbol{H}(\theta,\phi)$ are perpendicular to the direction of radiation $\hat{\boldsymbol{r}}$, they can then be obtained through the

following equations:

$$\begin{aligned} \boldsymbol{E}(\theta,\phi) &= -\,\mathrm{j}k\eta_0 \frac{\mathrm{e}^{-\mathrm{j}kr}}{4\pi r}\boldsymbol{F}_\perp(\theta,\phi) \\ \boldsymbol{H}(\theta,\phi) &= -\,\mathrm{j}k \frac{\mathrm{e}^{-\mathrm{j}kr}}{4\pi r}\hat{\boldsymbol{r}} \times \boldsymbol{F}_\perp(\theta,\phi) \end{aligned} \tag{2.1.2}$$

where $\boldsymbol{F}_\perp = \hat{\boldsymbol{\theta}}F_\theta + \hat{\boldsymbol{\phi}}F_\phi$, k is the free space wavenumber and η_0 is the free space impedance. The power density P_r can be found as the scalar value of the energy flux vector, corresponding to the power per unit area:

$$\boldsymbol{P} = \frac{1}{2}\mathrm{Re}\{\boldsymbol{E} \times \boldsymbol{H}^*\} = \hat{\boldsymbol{r}}\frac{1}{2\eta_0}|\boldsymbol{E}(\theta,\phi)|^2 = \hat{\boldsymbol{r}}\frac{\eta_0 k^2}{32\pi^2 r^2}|\boldsymbol{F}_\perp(\theta,\phi)|^2 = \hat{\boldsymbol{r}}P_r \tag{2.1.3}$$

where it can be noted that the radiated power attenuates with the square of the distance r. Further, the radiation intensity $U(\theta,\phi)$ is defined as the radiated power per solid angle, which can be found by removing the dependence on the distance from the power density P_r [5]:

$$U(\theta,\phi) = r^2 P_r = \frac{\eta_0 k^2}{32\pi^2}|\boldsymbol{F}_\perp(\theta,\phi)|^2 \tag{2.1.4}$$

By integrating the radiation intensity over all solid angles the total radiated power is obtained:

$$P_{\mathrm{rad}} = \iint U(\theta,\phi)\,\mathrm{d}\Omega = \iint U(\theta,\phi)\sin\theta\,\mathrm{d}\theta\,\mathrm{d}\phi \tag{2.1.5}$$

2.2 Gain, Directivity and Radiation Efficiency

The gain $G(\theta,\phi)$ is defined as the radiation intensity in an arbitrary direction, normalized with the power P_{acc} accepted by the antenna:

$$G(\theta,\phi) = \frac{U(\theta,\phi)}{P_{\mathrm{acc}}/4\pi} \tag{2.2.1}$$

where the 4π term takes into consideration an isotropic distribution of the accepted power. The directivity $D(\theta,\phi)$ is closely related to the gain, and is defined as the radiated power in an arbitrary direction, normalized with the total radiated power P_{rad} isotropically distributed:

$$D(\theta,\phi) = \frac{U(\theta,\phi)}{P_{\mathrm{rad}}/4\pi} \tag{2.2.2}$$

The radiation efficiency η_{r} is defined as the ratio of radiated power to the power accepted by the antenna, i.e.

$$\eta_{\mathrm{r}} = \frac{P_{\mathrm{rad}}}{P_{\mathrm{acc}}} \tag{2.2.3}$$

leading to the relation between gain and directivity being the following:

$$G(\theta,\phi) = \eta_{\mathrm{r}} D(\theta,\phi) \tag{2.2.4}$$

For antenna measurements, the gain is usually compared to that of an isotropic antenna, thus gain and directivity values are usually presented in decibels-isotropic (dBi), e.g. $G_{\mathrm{dBi}} = 10\log(G)$.

2.3 Radiation Pattern

The far-field radiation pattern of an antenna shows the angular distribution (θ, ϕ) of the radiated field strength, gain or directivity. Using spherical coordinates as depicted in Figure 2.1, there exist some principal planes that are used for two-dimensional visualization. The azimuthal pattern is the radiation shown in the x-y plane ($\theta = 90°$) and the elevation pattern is shown in a plane orthogonal to this, e.g. the x-z plane ($\phi = 0°$) or the y-z plane ($\phi = 90°$). The choice of elevation plane is usually determined from the purpose of achieving good illustrations. Moreover, the E- and the H-plane are commonly used planes for plotting the radiation pattern of some antennas. These are defined according to the IEEE Standard 145-1993 [4] as the planes containing the direction of maximum radiation and the E-field vector and H-field vector respectively.

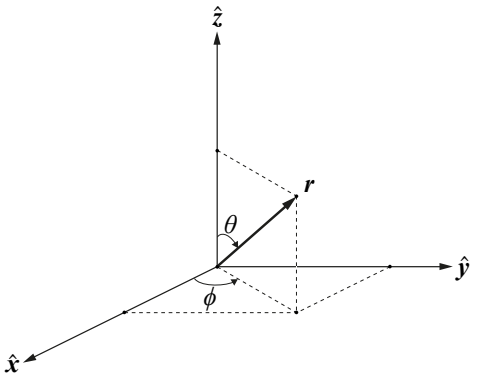

Figure 2.1: Spherical coordinate system for radiation pattern visualization.

In a specific pattern plane, the width of the radiation pattern can be described by the half-power beamwidth (HPBW), also called the 3 dB beamwidth. This is the angle between the two directions in which the radiated power is half of its maximum value, which expressed in dB-scale becomes $10\log(\frac{1}{2}) = -3\,\text{dB}$ decrease in power.

2.4 Bandwidth and Matching

An antenna can be seen as a load, introducing the frequency dependent input impedance of the antenna at its terminals as $Z_\text{a}(\omega) = R_\text{a}(\omega) + \text{j}X_\text{a}(\omega)$. The input resistance R_a is connected to different power loss mechanisms, while the reactance X_a is dependent on the reactive near-field. In order to achieve good performance, the matching between antenna and the feed network with reference impedance Z_0

should be made such that the reflection is minimized:

$$\Gamma(\omega) = \frac{Z_{\mathrm{a}}(\omega) - Z_0}{Z_{\mathrm{a}}(\omega) + Z_0} \tag{2.4.1}$$

The bandwidth can be seen as the frequency range around the center frequency f_{c} were the antenna performance is still acceptable. As the power accepted by the antenna can be expressed as

$$P_{\mathrm{acc}} = P_{\mathrm{in}}(1 - |\Gamma|^2) \tag{2.4.2}$$

the impedance bandwidth can be expressed as a return loss through the reflection coefficient in decibels:

$$\mathrm{RL}_{\mathrm{dB}} = -10\log|\Gamma|^2 = -20\log|\Gamma| \tag{2.4.3}$$

The impedance bandwidth can also be realized through the voltage standing wave ratio (VSWR):

$$\mathrm{VSWR} = \frac{1 + |\Gamma|}{1 - |\Gamma|} \tag{2.4.4}$$

Acceptable values are usually $\mathrm{VSWR} \leq 2 \Rightarrow |\Gamma| \leq 1/3$ which in decibel scale becomes $\mathrm{RL}_{\mathrm{dB}} \simeq -10\,\mathrm{dB}$. Hence, it is common to talk about the $-10\,\mathrm{dB}$ bandwidth when presenting simulated and measured performances. The impedance bandwidth ($\mathrm{VSWR} \leq S$) is also related to the total Q-factor (see Section 2.7) according to [6]:

$$\mathrm{FBW} = \frac{S - 1}{Q_{\mathrm{tot}}\sqrt{S}} \tag{2.4.5}$$

where FBW is the fractional bandwidth, which is the ratio between the frequency range with acceptable performance with respect to the center frequency:

$$\mathrm{FBW} = \frac{f_{\mathrm{max}} - f_{\mathrm{min}}}{f_{\mathrm{c}}} \tag{2.4.6}$$

2.5 Mutual Coupling

For array configurations, the introduction of multiple antenna elements gives rise to mutual impedance between the different elements. The scattering matrix can be used to characterize the matching for each port network and the mutual coupling between every element. For n number of antennas the scattering matrix is:

$$\begin{pmatrix} \mathrm{b}_1 \\ \mathrm{b}_2 \\ \vdots \\ \mathrm{b}_n \end{pmatrix} = \begin{pmatrix} S_{11} & S_{12} & \cdots & S_{1n} \\ S_{21} & S_{22} & \cdots & S_{2n} \\ \vdots & \vdots & \ddots & \vdots \\ S_{n1} & S_{n2} & \cdots & S_{nn} \end{pmatrix} \begin{pmatrix} \mathrm{a}_1 \\ \mathrm{a}_2 \\ \vdots \\ \mathrm{a}_n \end{pmatrix} \tag{2.5.1}$$

where a_i represents the incident signal and b_i the reflected signal at port i respectively. Thus S_{ii} represents the reflection coefficient for antenna i as in (2.4.1), and the mutual coupling loss between two arbitrary ports is described by the respective off-diagonal elements.

2.6 Antenna Scaling

A general rule regarding antenna dimensions can be applied considering re-designing certain antennas at other center frequencies. If an antenna with length l_1 is resonant at $f = f_1$ and it is desirable to have resonance at $f = f_2$, then an approximate resonant length l_2 can be found through:

$$l_2 = l_1 \frac{f_1}{f_2} = l_1 \frac{\lambda_2}{\lambda_1} \tag{2.6.1}$$

e.g. if an antenna resonant at 30 GHz has a footprint of $20 \times 10\,\mathrm{mm}^2$, the same design can be resonant at 15 GHz if the size is doubled, i.e. $40 \times 20\,\mathrm{mm}^2$. Note that this does not always apply, and should be used more for a rough first re-design and to get an idea of an antennas dimensions at another operational frequency.

2.7 Q-factor

The Q-factor is another parameter that is of great significance when evaluating the performance of an antenna. For every mechanism that introduces a power loss P_i, there is a corresponding quality factor Q_i and they are related through:

$$P_i = \frac{2\omega W_{\mathrm{M,E}}}{Q_i} \tag{2.7.1}$$

where $W_{\mathrm{M,E}}$ is the maximum stored energy (magnetic W_{M} or electric W_{E}) at resonance ω. Hence, the radiated power P_{rad} is related to Q_{rad} through (2.7.1), and the total Q_{tot} of a system can be expressed as:

$$P_{\mathrm{tot}} = \sum_i P_i \quad \Rightarrow \quad \frac{1}{Q_{\mathrm{tot}}} = \sum_i \frac{1}{Q_i} \tag{2.7.2}$$

Furthermore, from the total quality factor Q_{tot} one can show a relation to the impedance bandwidth as in (2.4.5), hence the Q-factor relates to both the radiated power P_{rad} and thus the radiation efficiency η_r, and the bandwidth, making it a very useful parameter for measuring loss mechanisms.

2.8 Ohmic Losses

Power losses in materials can be caused by both the dielectric and conductive properties of the material. The magnitude of these losses, often called ohmic losses, is usually presented as the loss tangent:

$$\tan\delta = \frac{\varepsilon''}{\varepsilon'} \tag{2.8.1}$$

where ε' and ε'' are the frequency-dependent real- and imaginary part of the complex permittivity ε:

$$\varepsilon = \varepsilon_0 \varepsilon_{\mathrm{r}} = \varepsilon_0(\varepsilon'_{\mathrm{r}} - \mathrm{j}\varepsilon''_{\mathrm{r}}) \tag{2.8.2}$$

here, ε_0 is the vacuum permittivity and ε_r is the relative permittivity. A conductive material is characterized by a large conductivity, so that the loss tangent for such materials can be found through:

$$\varepsilon_\mathrm{r} = \varepsilon_\mathrm{r}' - \mathrm{j}\frac{\sigma}{\omega\varepsilon_0} = \varepsilon_\mathrm{r}' - \mathrm{j}\frac{1}{\omega\rho\varepsilon_0} \tag{2.8.3}$$

where σ and ρ are the conductivity and resistivity of the material respectively. Since the losses are frequency-dependent, the loss tangent should if possible be presented at the measurement frequencies, e.g. something like $\tan\delta = 0.0035$ at $10 - 40\,\mathrm{GHz}$.

2.9 Surface Wave Losses

When considering antennas mounted on top of a substrate, surface waves will be excited if the relative permittivity $\varepsilon_\mathrm{r} \geq 1$. Surface waves are waves guided by the substrate due to total internal reflection, and are reflected at the ground plane and air-substrate interface respectively.

The guided waves cause coupling to other nearby elements, and diffract at the edges of the substrate causing an unwanted total radiation pattern [6]. Furthermore, the power losses occurring in the substrate decrease the radiated power of the antenna. As ε_r and h are increased, the attenuation becomes more severe and the power losses increase. The lowest order mode, the TM_0-mode, will always occur as its cutoff frequency $f_\mathrm{co} = 0$, however higher order modes can be avoided by choosing appropriate substrate thickness according to:

$$f_\mathrm{co} = \frac{nc}{4h\sqrt{\varepsilon_\mathrm{r} - 1}} \tag{2.9.1}$$

where c is the speed of light in vacuum, h is substrate thickness and n corresponds to the mode number (TE: $n = 1, 3, 5, ...$ and TM: $n = 0, 2, 4, ...$). Thus, by choosing a thickness as

$$\frac{h}{\lambda_0} \leq \frac{1}{4\sqrt{\varepsilon_\mathrm{r} - 1}} \tag{2.9.2}$$

only the TM_0-mode will exist. According to [6] surface wave losses can be neglected when

$$\frac{h}{\lambda_0} \leq \frac{0.3}{2\pi\sqrt{\varepsilon_r}} \tag{2.9.3}$$

2.10 Arrays

The use of array configurations of antennas makes it possible to not only increase the total gain by using many elements, but also radiate power in a desired angular direction (a phased array system), hence it is a fundamental part within the antenna design topic. An array configuration of identical elements with equal spacing introduces the array factor, from which the total far-field radiation of the

array can be found from the radiation vector of the basic element, $\boldsymbol{F}_{\mathrm{s}}(\theta,\phi)$, such as:

$$\begin{aligned}\boldsymbol{F}_{\mathrm{tot}}(\theta,\phi) &= A(\theta,\phi)\boldsymbol{F}_{\mathrm{s}}(\theta,\phi) = \sum_{n=1}^{N} a_n \mathrm{e}^{\mathrm{j}\boldsymbol{k}\cdot\boldsymbol{d}_n}\boldsymbol{F}_{\mathrm{s}}(\theta,\phi) \\ \text{with } \boldsymbol{k} &= (k_x,k_y,k_z) = \hat{\boldsymbol{x}}k\cos\phi\sin\theta + \hat{\boldsymbol{y}}k\sin\phi\sin\theta + \hat{\boldsymbol{z}}k\cos\theta\end{aligned} \tag{2.10.1}$$

Here, N is the total number of elements in the array, $\boldsymbol{d}_n$ is the displacement vector and a_n is the feed coefficient of the respective element. The radiation intensity of the array can be found from $\boldsymbol{F}_{\mathrm{tot}}(\theta,\phi)$ in a similar way as in (2.1.4). It can be seen that only the far-field radiation of the basic element has to be calculated, while the array factor takes into account the combining of the radiating elements and thus the overall radiation pattern. It can also be seen that the increase in gain, compared to a single antenna, can be found through the array factor where the feed coefficients and the phase of these determine the overall contribution. Maximum additional gain can be approximated by multiplying by the number of elements used in the array, i.e. $+10\log(N)$ dB ($N = 2$ corresponds to approximately $+3$ dB). For illustration purposes, let the array be one dimensional in the $\hat{\boldsymbol{z}}$-direction, with equal spacing d between every element as seen in Figure 2.2. The array factor can then be rewritten as

$$\begin{aligned}A(\theta,\phi) &= \sum_{n=1}^{N} a_n \mathrm{e}^{\mathrm{j}\boldsymbol{k}\cdot\boldsymbol{d}_n} = \sum_{n=1}^{N} a_n e^{\mathrm{j}nkd\cos\theta} = \sum_{n=1}^{N} a_n e^{\mathrm{j}n\Psi} = A(\Psi) \\ \Psi &= kd\cos\theta\end{aligned} \tag{2.10.2}$$

where the incremental phase shift, $\Psi = kd\cos\theta$, has been defined. The two-dimensional array case can be derived in similar manner.

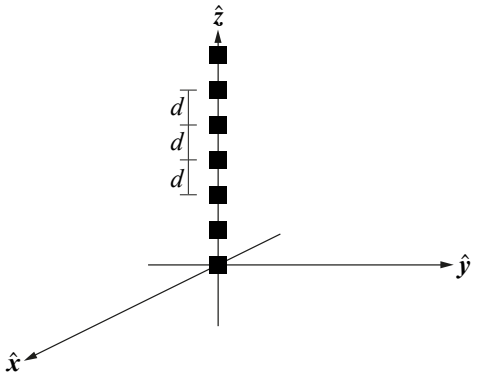

Figure 2.2: One dimensional array with spacing d along the $\hat{z}$-direction.

2.10.1 Phased Array

A phased array can be constructed by changing the feed coefficients a_n of the array elements using a translation of Ψ. Initially, the array has its maximum gain when the exponential in the array factor is zero, i.e. $\max\{A(\Psi)\}= |A(0)|$. This occurs, for an array along the $\hat{\boldsymbol{z}}$-direction (as seen in Figure 2.2), when $\theta = 90^\circ$ and a_n is independent of n. However, changing the coefficients a_n according to

$$a_n' = a_n \mathrm{e}^{-\mathrm{j}n\Psi_0} \tag{2.10.3}$$

will change the direction of maximum radiation:

$$A'(\Psi) = \sum_{n=1}^{N} a_n' \mathrm{e}^{\mathrm{j}n\Psi} = \sum_{n=1}^{N} a_n \mathrm{e}^{\mathrm{j}n(\Psi-\Psi_0)} = A(\Psi - \Psi_0) \tag{2.10.4}$$

The new maximum is now found when $\Psi - \Psi_0 = 0$, e.g. for the case of a one-dimensional array just as above when:

$$\begin{aligned} \Psi - \Psi_0 &= kd(\cos\theta - \cos\theta_0) = 0 \\ \Rightarrow \theta_0 &= \theta \end{aligned} \tag{2.10.5}$$

The beam have thus been steered towards θ_0 by changing the phase of the feed with Ψ_0.

2.10.2 Spacing Between Elements

The incremental phase shift Ψ is defined between two angular ranges. From $\mathrm{e}^{-\mathrm{j}n\Psi}$ it is 2π-periodic between $-\pi \leq \Psi \leq \pi$, however from its definition (2.10.2) the periodicity depends on the choice of element spacing:

$$-kd \leq \Psi \leq kd \tag{2.10.6}$$

If $kd > \pi$ the values of $A(\theta, \phi)$ will be over-specified and give rise to grating lobes, which are lobes in undesired directions. Similarly, if $kd < \pi$ the values of $A(\theta, \phi)$ will be under-specified. The element spacing is thus often chosen such that the whole range of variation is covered, i.e. since k is the free space wavenumber:

$$\begin{aligned} kd &= \frac{2\pi d}{\lambda} = \pi \\ \Rightarrow \quad d &= \lambda/2 \end{aligned} \tag{2.10.7}$$

where λ is the free space wavelength.

Chapter 3

State of the Art in mmWave Antennas

3.1 Performance and Characteristics Targets of the Study

A lot of studies have already been carried out regarding different antenna types in the millimeter range. There exist numerous areas of applications that might benefit from the use of millimeter wave (mmWave) devices in wireless communications.

In particular a lot of research has been focused around the 60 GHz frequency band (also called the V-band). This is mainly because the band is unlicensed with a very wide bandwidth, thus enabling the possible increase of achieved data rates. However, the free space loss is more severe when moving to higher frequencies, and 60 GHz also occurs at an atmospheric absorption peak, limiting the possible transmission distances even more. Therefore, the usage of 60 GHz has been narrowed down to applications with very small cell sizes, e.g. wireless local area network (WLAN) and wireless personal area network (WPAN), where the wide bandwidth can be exploited despite the obvious disadvantages of limited distances. Hence, a major part of the encountered literature is focused around antennas operating at 60 GHz, but nevertheless a lot of insight can be made on the performances of these, to later be scaled down to the operating frequencies of interest (15 GHz and 28 GHz).

For commercial purposes, the use of expensive and bulky antenna types are highly inappropriate. Thus, even though reflector-, lens and horn antennas have good radiation properties at mmWave frequencies, they suffer from these disadvantages making them not as suitable for cellphone applications [7]. Instead, since inexpensive manufacturing is one of the key points for commercial usage, it can be seen that a lot of focus is held around finding solutions that are cheap to manufacture and low in profile.

In summary, the antenna types should satisfy a wide bandwidth (> 500 MHz) to exploit the bandwidth available, high radiation efficiency ($\eta_{\mathrm{r}} > 50\,\%$) to avoid as much losses as possible in the antenna element, be small in size to enable arrays to be implemented on the mobile station and be realizable through low-cost fabrication processes to enable mass production.

Having said all this, what follows below is an overview of the state of the art regarding mmWave antennas, where a focus around 60 GHz antennas are obvious in its presence. This overview provides a good motivation for drawing the initial conclusion regarding what antennas to consider for further evaluation.

3.2 Antenna on chip

Antenna on chip (AoC) indicates the integration of an antenna on the same chip as other circuits using standard technologies (e.g. III-V, CMOS or SiGe) [7]. Using antenna types that have sizes in the order of the operating wavelength enables this integration when moving up towards the mmWave frequencies. The reason why more and more research is being done within the area is that by removing all connections between the RF circuit and the radiating element, a significant cost reduction can be realized [8]. By producing the antenna in the same process as the rest of the circuit, several manufacturing issues can be removed, while simultaneously suppressing losses that would otherwise occur in the complex interconnections [9]. It is seen that the on chip antenna solution is still under development, and has not come far enough to enable performances meeting the requirements for commercial usage. In general, the AoCs have both very low radiation efficiency and gain.

The most common types of on chip antennas are printed antennas (Section 3.4), since these are suitable for integration with solid-state devices, but a certain amount of dielectric resonators (Section 3.5) have also been encountered. The integrated circuits (IC) used for GHz radios are traditionally designed using III-V technology such as gallium arsenide (GaAs) or indium phosphide (InP). However for commercial purposes the need for a more low cost solution is essential, which implies that silicon (Si) technology should be used instead [7]. In III-V ICs, a ground plane is usually present which enables the use of patches that are well-documented antennas with generally good performance. However this is not the case for Si technology [10], where a ground plane is usually avoided. Due to this, most encountered research has been done using other printed antenna types such as dipoles and travelling wave antennas [9–11]. General values of gain and radiation efficiency for AoCs are around $G \sim 0\,\mathrm{dBi}$ and $\eta_r \sim 10\,\%$ respectively. Results for encountered individual AoCs will be illustrated in a later table (Table 3.1). A typical model of an antenna mounted on a Si IC chip can be seen in Figure 3.1.

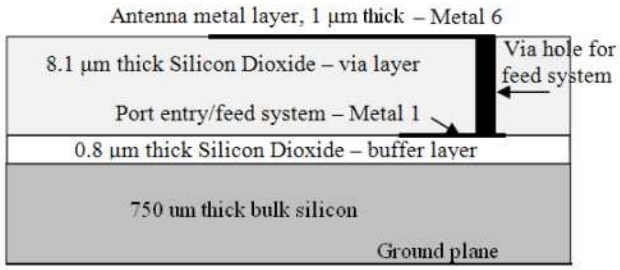

Figure 3.1: Cross sectional view of a typical IC model for antenna on chip simulation set up [9] © 2009 IEEE.

3.2.1 Concerns and Improvement Techniques

The major concern regarding on chip antennas is the low radiation efficiency, i.e. most of the power is lost in other mechanisms than radiation. Commercial Si substrates have a relatively low resistivity ($\rho \approx 10-20\,\Omega \cdot \mathrm{cm}$) which causes ohmic losses in the substrate (Section 2.8) and hence reduce the radiation efficiency. These losses can be reduced by using selective ion- or proton implantation [7] which increases the resistivity, however this directly indicates an increased cost. Moreover, losses also occur due to power trapped in surface waves (Section 2.9). This does not only reduce the radiation efficiency, but also introduces mutual coupling. Due to the fact that the circuit and the antenna are in close vicinity of one another, mutual coupling occurs between the antenna and other components (power lines, capacitors etc.) causing detuning of the different components. This is a major drawback in performance, and in order to suppress these interferences one needs to understand the different coupling mechanisms. Suitable architecture and the use of ground shields have been shown to reduce the cross talk [10]. Substrate thinning and the use of substrates with low dielectric constant, see (2.9.3), can help to reduce the power lost through surface waves. However, the substrate is of silicon with $\varepsilon_r = 11.9$, and the use of lower permittivity materials will probably be limited to the use of the top, insulating layer. The most commonly used insulating material is silicon dioxide (SiO_2) with $\varepsilon_r = 3.9$, but proposals have been made using thin layers of BCB ($\varepsilon_r = 2.7$, $\tan\delta = 0.0008$) on top for efficiency enhancement [10]. Micromachining techniques such as wet- or dry etching[1] can also be used to remove substrate in order to reduce losses. However, dry etching is needed to perform an isotropic etch with good resolution, which requires expensive equipment.

For the reader interested in finding out more about AoCs, the work presented in [10] is recommended.

3.3 Antenna in Package

The antenna in package (AiP) solution indicates that an antenna or an array of such is put in the same chip package as the radio frequency (RF) die. By using multilayer techniques, an antenna can be integrated in the package, which in turn offers more degrees of freedom regarding the design complexity. An example of an AiP solution is shown in Figure 3.2. The feeding network can be integrated within the layers, and different enhancement techniques can be implemented by controlling each layer. Because of this, many AiPs have shown good performances in terms of bandwidth and gain. Interconnection between the chip and the package can then be established by either wire bonding or flip-chip bonding. By having the freedom to place the RF die almost arbitrarily, one can minimize the impact the active devices in the chip have on the antenna performance. The available volume and area for antenna implementation is not as restricted as for AoCs, which makes array configurations compatible. Also, compared to on chip antennas a broader variety of different antenna types have been presented for the in package solution, mainly due to the flexibility that applies to multilayer structures. Thus,

[1] The fundamentals about etching- and implantation methods can be found in [12].

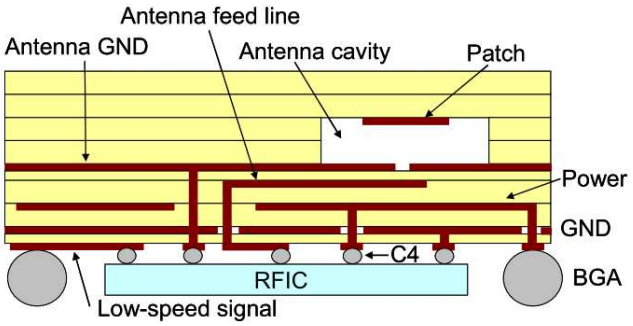

Figure 3.2: Cross sectional view of LTCC multilayer packaging with in package patch antenna [13] © 2010 IEEE.

the antenna types that have been encountered are more focused around the certain types that have shown good performance in the millimeter range and are not as restricted to outside factors. Examples of such antennas are printed antennas such as patches and dipoles, substrate integrated waveguides (SIW), slots and microstrip grid antennas [2]. Results for encountered individual AiPs will therefore be embedded with other illustrated results in the upcoming sections.

3.3.1 Concerns and Improvement Techniques

In package antennas have in general shown good performance in terms of gain and bandwidth [7], and the concerns seem to be more about obtaining structures that are not too complex. In order to integrate an antenna in a package a multilayer technology is needed, and these are limited with specific restrictions for each technology. The most common materials are different kinds of polymers, ceramics and teflon which all have relatively good properties at high frequencies. The process technologies associated with the polymer and ceramic materials are low-temperature cofired ceramic (LTCC) and liquid crystal polymer (LCP) respectively [2]. One of the difficulties with AiPs is the interconnection between the die and the package. Interconnections are usually made through wire bonding or flip-chip bonding[2], where wire bonding is the more commercially used. The wire-bonding technique is robust and inexpensive, but the long wires introduced act as inductors and affect the performance of the whole system. This effect can be suppressed by using the more expensive flip-chip technique instead, which results in less series inductance as the bumps are shorter and thicker than the wires [2]. Apart from this, the main issues of in package antennas are more related to the actual package design [13]. The layer stack-up should not be too complicated to achieve well enough mechanical and electrical reliability, and at the same time be possible to manufacture using not too expensive assembly processes.

Having briefly introduced the concepts of two new antenna integration techniques for mmWave frequency operation, it is time to evaluate the different encountered antenna types from a performance point of view. Hence, improvement

[2]The fundamentals about bonding techniques can be found in [12].

techniques that are more connected to the antenna element in itself will be presented simultaneously with related articles in the upcoming section.

3.4 Printed Antennas

Printed antennas are in its simplest form inexpensive to fabricate, low in profile and light in weight. In general they are produced by standard lithographic processes, where metal is printed on top of a substrate. Moreover, their size is in the order of the resonance wavelength, which make them array compatible to obtain higher gain values, but also opens up new integration options (see Section 3.2 and 3.3) at mmWave frequencies. Due to these properties they are highly suitable for commercial use and are frequently occurring antenna types on the research front. The most common types of printed antennas are patches, dipoles and variations of these, as shown in Figure 3.3. Presenting the different printed antenna types

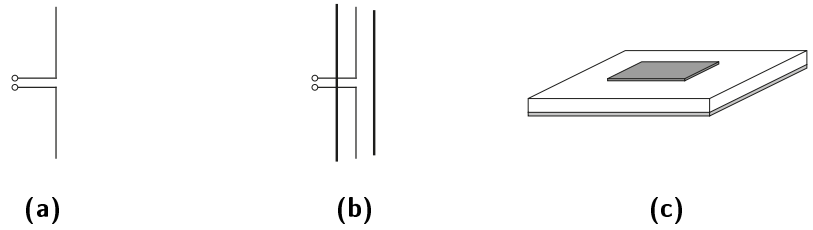

Figure 3.3: Different kinds of printed antenna types. (a) a dipole antenna, (b) a yagi antenna, (c) a rectangular patch antenna.

shortly, a dipole is one of the most common types of antennas and exist in numerous variations. A dipole antenna consists of two conductive elements, usually metal wires with a small radius, as shown in Figure 3.3a. Current is fed in the center. Most commonly, the length of the dipole is half an operational wavelength (half-wave dipole) which results in a current distribution with zero values at the end points and maximum in the center. The radiation is omnidirectional with maximum in the direction perpendicular to the dipole axis, i.e. it is donut-shaped with the hole axis in the direction of the dipole. The maximum directivity of a half-wave dipole is 2.15 dBi.

A common variation of a dipole antenna is the folded dipole, which is a half-wave dipole with an additional wire connecting the two ends to increase the radiation resistance [5]. Another one is the yagi antenna, as seen in Figure 3.3b, which uses one current-fed dipole element, together with a selected amount of parasitic directors and/or reflectors. The directors are slightly shorter than the driven element while the reflector is slightly longer. The parasitic elements helps to direct the radiation in the direction of the director. Using more elements indicates more increase in gain from the parasitic array configuration, e.g. in [5] using one reflector, one driven half-wave dipole and one director a total gain of 8.18 dBi was simulated, indicating an increase of $8.18 - 2.15 = 6.03$ dBi compared to a single half-wave dipole.

The patch antenna, which is simply a metal patch on top of a substrate layer with an underlying ground plane as seen in Figure 3.3c, is another common printed antenna type. Various shapes exist, where a rectangular or circular patch are the most common ones. The patch is resonant at approximately half a wavelength in the substrate. Excluding the feed network, degrees in freedom exist in the choice of dielectric constant of the substrate ε_r, height of the substrate h and length L and width W or radius r of the patch respectively. Usual maximum gain values are between 5 and 7 dBi with a broadside radiation, i.e. the radiation is maximum in the upward direction perpendicular to the patch.

Type [ref.]	Freq. (GHz)	Gain (dBi)	BW (GHz)	Rad. Eff. η_r
Dipole on Chip [9]	60	-6.7	-	9 %
Yagi on Chip [9]	60	-3.6	-	15.8 %
Yagi on Chip [11]	60	-10	10	10 %
Folded Dipole in Package, LTCC [14]	60	8	7.8	90 %
Yagi in Package, LTCC [15]	60	6	2.3	93 %

Table 3.1: Summary of printed antennas other than patches. BW denotes the -10 dB bandwidth.

Type [ref.]	Freq. (GHz)	Gain (dBi)	BW (GHz)	Rad. Eff. η_r
Aperture-Coupled, Air Cavity in Package [13]	60	-	5	-
4x6 Array, Parasitic, LTCC [16]	60	15.5	9	-
Aperture-Coupled, Superstrate, LTCC [17]	60	7	9	-
4x4 Array, Aperture-Coupled, Air Cavity, LTCC [18]	60	18.2	7	-
Aperture-Coupled, Parasitic, LTCC [19]	77	8	4	80 – 90 %
Aperture-Coupled, Superstrate [20]	60	7.8	4	90 %
Air Cavity [21]	60	8.7	5.8	96 %

Table 3.2: Summary of patch antennas. BW denotes the -10 dB bandwidth.

Research results from printed antennas for millimeter wave applications can be seen in Table 3.1 and 3.2. It is noticeable that the on chip printed antennas have

both low radiation efficiency and negative gain just as mentioned earlier (Section 3.2, p. 14). It seems that when moving away from the on chip solution, patch antennas are the printed antenna type where the most extensive studies have been carried out, where also good performances have been obtained. Furthermore and equally important, array configurations are made realizable when the dimensional restrictions of on chip solutions are relaxed. Table 3.2 is a summary of encountered articles on patch antennas for visualization purposes of different enhancement techniques.

From Table 3.2 it can be seen that aperture-coupling seems to be a recurring feeding technique for patch antennas [13, 17–20]. This technique couples the energy from the transmission line to the antenna through a slot in the ground plane. Advantages with this are the isolation of the radiating element and that optimization can be done independently for antenna and feed network respectively. Moreover, it is noticeable that enhancement techniques are extensively used as multilayer technologies enables the implementation of them.

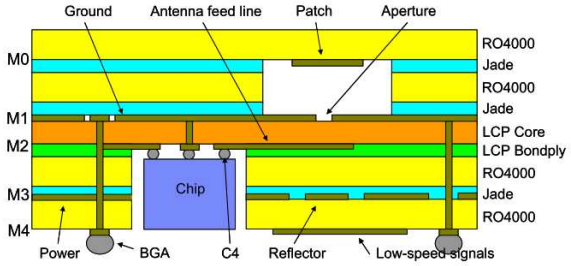

Figure 3.4: Multi-layer stack-up for aperture-coupled air cavity patch [13] © 2010 IEEE.

In Figure 3.4 a cross section of the solution proposed in [13] is shown. The multilayer was realized through LTCC technology and uses an aperture-coupling to excite the patch antenna. The use of an air cavity suppresses losses due to surface waves while improving the obtained bandwidth. Since surface waves exist for $\varepsilon_r > 1$, these can be suppressed by choosing air as the substrate material. The antenna is then attached on the bottom of a substrate layer placed on top, thus the name superstrate. The folded dipole in [14] shows relatively good performance, resembling the performances of different patches but with a dipole radiation pattern. An air cavity and metal fencing, which can suppress the surface wave losses, are employed to enhance the antenna. The circular patches in [16] are also employed with metal fencing, together with parasitic elements. By adding parasitic patches that resonate close to the driven patch the bandwidth can be increased. These parasitic elements can be placed above and around the driven element. A lot of research has been done using LTCC as in package implementation technique [16–19], where the LTCC tape Ferro A6 is used as substrate ($\varepsilon_r = 5.8 - 5.9$, $\tan\delta = 0.001 - 0.002$ at $f \leq 40$ GHz) [22]. LTCC is however a relatively expensive technology, that might restrict its usage to the research front and not commercial use [13]. The stack-up proposed in [13] uses RO4000 laminates instead ($\varepsilon_r = 3.55$ at $f = 8 - 40$ GHz and $\tan\delta = 0.0027$ at $f = 10$ GHz) [23], which enables the use of

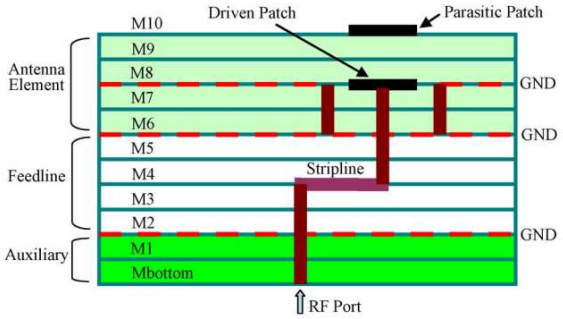

Figure 3.5: Circular patch with parasitic element and metal vias fence [16] © 2011 IEEE.

standard printed circuit board (PCB) processes more suitable for mass production.

3.5 Dielectric Resonator Antennas

A dielectric resonator antenna (DRA) consists of a substrate material with high permittivity, that act as a resonant cavity and radiates as power leaks from the resonant structure. The most common shapes of DRAs are rectangular, cylindrical and hemispherical, as seen in Figure 3.6. Their small size (less than a wavelength in the substrate) and simple structure make them good candidates for mmWave wireless communications, as they are still realizable through low-cost fabrication. DRAs have been shown to be good radiators at high frequencies, with high ra-

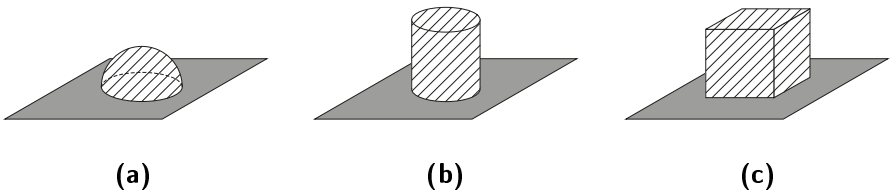

Figure 3.6: Different shapes of DRAs. (a) a hemispherical DRA, (b) a cylindrical DRA, (c) a rectangular DRA.

diation efficiency and broad bandwidth. DRAs are usually mounted on top of a ground plane, resulting in a radiation pattern similar to the one from a printed patch antenna, with maximum radiation straight up from the structure. Usual maximum gain are in the order of that of a patch antenna ($5 - 7\,\mathrm{dBi}$). Some encountered research results are listed in Table 3.3. Note that in [24] an on chip DRA is proposed, and that the antenna has better presented performance than the printed AoCs in Table 3.1. The author, P. V. Bijumon, has also published several other papers on DRAs as on chip solutions. The proposed solutions of DRAs instead of printed antennas on chip, is due to the possible reduction of substrate losses, higher radiation efficiencies and wider bandwidth [24]. From Table

Type [ref.]	Freq. (GHz)	Gain (dBi)	BW (GHz)	Rad. Eff. η_r
Rectangular on Chip [24]	60	5.3	1.9	89 %
2x1 Array, Aperture-Coupled, Cylindrical [25]	60	8.25	9	98 %
SIW-slot, Rectangular [26]	37.5	5.5	-	95 %
SIW-slot, Cylindrical [27]	60	5.5	13	$80 - 92$ %

Table 3.3: Summary of DRAs. BW denotes the -10 dB bandwidth.

3.3 it is noticeable that the performances of presented DRAs have maximum gain comparable to the patches presented in the above section. The radiation efficiency η_r can be seen to be generally quite high, around 90 %, and the antennas [25, 27] achieve around ~ 6 % bandwidth. The DRAs in [25–27] all exploit the use of a slot to couple the energy from the feed network. The proposed design in [25] use an aperture-coupling, the same as in above presented patches [13, 17–20], and can be seen in Figure 3.7.

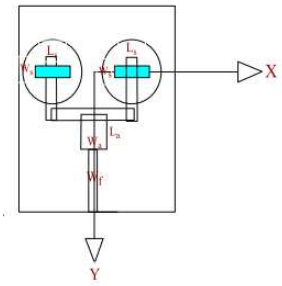

Figure 3.7: Top view of a 2×1 array of aperture-coupled cylindrical DRA [25]. The turquoise shows the aperture © 2012 IEEE.

The proposed designs in [26, 27] use a different kind of slot coupling. Instead of a transmission line, a substrate integrated waveguide (SIW) is used as feeding line. The SIW approach can be realized with standard PCB processes, and antennas based on SIWs have also been proposed (see Section 3.6). The design model from [26] is visible in Figure 3.8. The three designs in [25–27] all use a substrate for the DRA with permittivity of $\varepsilon_{dr} = 10.2$ (Rogers RT 6010 or RT TMM10i), with the feed beneath the ground plane etched in Rogers RT Duroid 5870/80 ($\varepsilon_r = 2.33/2.20$ and $\tan\delta = 0.0012/0.0009$ at $f = 8 - 40$ GHz) [23].

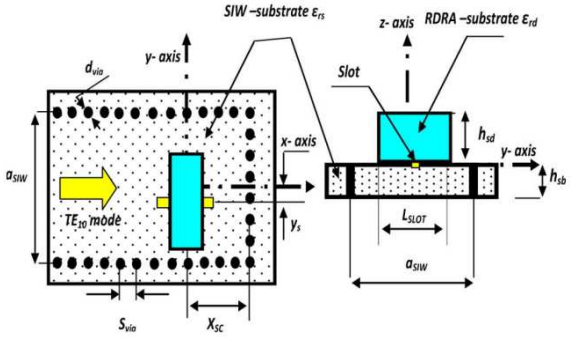

Figure 3.8: Rectangular DRA fed by a SIW through a slot in the top ground plane [26]. The yellow shows the aperture © 2010 IEEE.

3.6 Substrate Integrated Waveguide Antennas

Substrate integrated waveguide (SIW) is a technique that can be employed to construct integrated antennas. The general appearance of a SIW circuit are a dielectric layer between a top- and bottom metal clad while rows of metalized via holes act as side walls. This can be seen in Figure 3.8 as the feeding mechanism for the DRA. SIWs can be realized through low-cost standard PCB processes making it possibly suitable for mass production. However, the use of SIW technology is not only restricted to antenna construction, but its advantages are more related to the possibility of integrating an antenna with other circuits on a single substrate [28]. Thus, many encountered design proposals address an antenna together with a beamforming network (BFN). The BFN is the network that provides the beam-steering and beamforming if an array configuration is used. Examples of such are a Butler matrix, a Rotman lens or a phased array.

Type [ref.]	Freq. (GHz)	Gain (dBi)	BW (GHz)	Rad. Eff. η_r
Linearly Tapered Slot [29]	36	10.6	7	57.5 %
Linearly Tapered Slot, 4x1 Array [30]	33.5	10.3	-	68 %
Slot, 12x12 Array [31]	60	22	2.5	68 %
Slot, 8x8 Array [32]	95	18.95	3.56	57 %
H-plane Horn, Open-ended [33]	28	5.75	1	-

Table 3.4: Summary of SIW antennas. BW denotes the $-10\,\mathrm{dB}$ bandwidth.

Encountered research results are listed in Table 3.4. The presented results show radiation efficiencies that are lower than those from DRAs, however high

gain values are obtained as large array configurations have been realized.

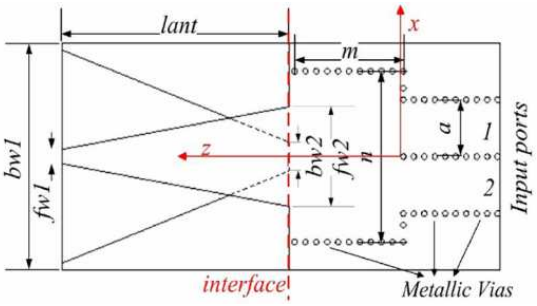

Figure 3.9: Linearly tapered slot antenna using SIW technology [29]

In [29] a linearly tapered slot antenna using SIW technology is presented. A single substrate Rogers RT Duroid 5880 with a permittivity of $\varepsilon_r = 2.2$ is used. The design can be seen in its planar cross section in Figure 3.9, where the left part is the radiating element and the right part is a multimode feeding network. The antenna array, at the far left in the figure, is realized by cutting away selected parts of the top- and bottom metal respectively. The antenna is a modified version of a vivaldi radiator and radiates with a main lobe in the planar direction containing the tapering, which is seen in Figure 3.9 as the $\hat{\boldsymbol{z}}$-direction. The antenna achieved high gain 10.6 dBi and a large bandwidth but a low radiation efficiency. The size however is relatively big for mobile implementation purposes. At a center frequency of 36 GHz the antenna element is $17.4 \times 15\,\mathrm{mm}^2$.

In [30] a multibeam antenna integrated with an asymmetrical BFN is presented. The design is a further development of the antenna in [29], and have thus the same characteristics. A single substrate Rogers RT Duroid 5880 with a permittivity of $\varepsilon_r = 2.2$ is used. The BFN consists of an amplitude transformation part (H-plane moder) and a phase transformation part (Multimode SIW) and the whole design can be seen in Figure 3.10. The article is mostly focused on how the whole integrated structure is realized, and not so much on the performance of the antenna element. Maximum gain values are presented for different frequencies by excitations from the 4 ports, which all lie in the vicinity of the gain value in Table 3.4. The size of the antenna element is $14 \times 20\,\mathrm{mm}^2$, and the total size including the BFN is around $34 \times 20\,\mathrm{mm}^2$.

Both the antennas in [31, 32] are based on the same principle, where the radiation arise from slot apertures in the top metal layer, with high achieved gain. Both antennas use Rogers RT Duroid 6002 with $\varepsilon_r = 2.94$. The antenna from [31] can be seen in Figure 3.11. The array consists of 12 waveguides with 12 slots each, and similarly for the array in [32] but with 8 waveguides. It is necessary to have waveguides of long enough lengths to realize this kind of slot radiation, as all the power transferred to the waveguide need to be radiated and/or attenuated before it reflects back to the feed network. Thus, the size becomes quite big consisting of many slot elements. The 8×8 array in [32] is $20 \times 15\,\mathrm{mm}^2$ and operates at 95 GHz. The slot spacing is half a guided wavelength at desired center frequency to achieve

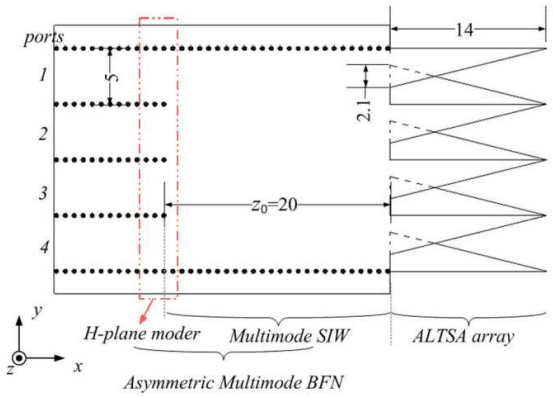

Figure 3.10: SIW multibeam antenna with asymmetrical BFN on a single substrate [30] © 2011 IEEE.

in-phase excitation of all slots. The main difference between the two designs is the feeding network approach. In [31], a primary transition from a 50-Ω co-planar waveguide to the SIW is made, the SIW then bends and T-junctions are made for the waveguides. In [32] the feed network consists of microstrip T-junctions which then feed each waveguide through a tapered microstrip transition. These SIW slot antennas radiate straight upwards seen from the structure.

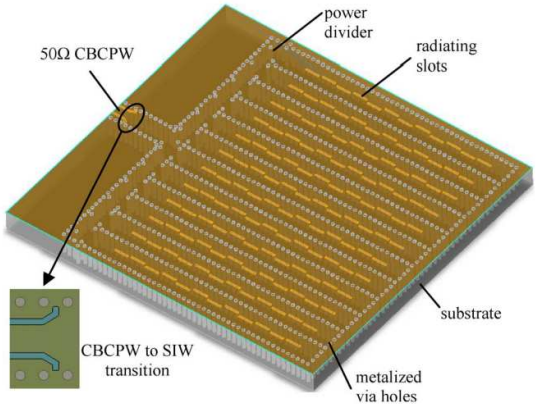

Figure 3.11: 12×12 SIW slot antenna array [31] © 2010 IEEE.

The H-plane horn in [33] can be seen in Figure 3.12 in its planar cross section. The substrate used has a permittivity of $\varepsilon_r = 4.8$ and the horn is fed through a probe as seen in the figure. That the horn is of H-plane type means that the tapering is only done in the planar cross section. The width of the waveguide is 5 mm and the width of the horn aperture is 14 mm. The total footprint of a single element is $16.8 \times 14\,\mathrm{mm}^2$. The authors present the optimized design when

a dielectric slab (rectangular and elliptic) is applied at the aperture of the horn, which can be used to achieve a more narrow beam and thus a higher maximum gain. The gain value presented in Table 3.4 is the achieved gain without any dielectric load, and the gain was increased significantly by using dielectric loads of different sizes and shapes. Results from a dielectrically loaded 4×1 array were also shown, with a measured maximum gain of 13.75 dBi. The antenna radiates with maximum directivity in the direction of the open end.

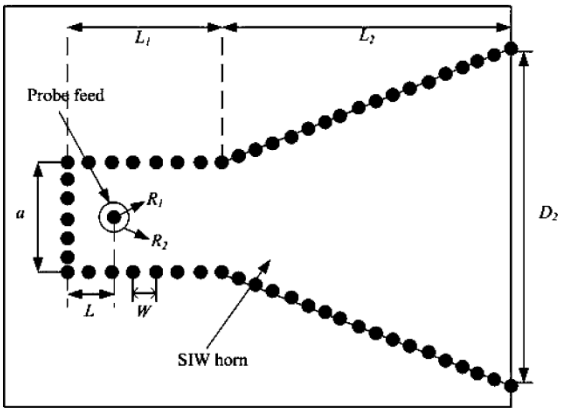

Figure 3.12: SIW H-plane horn antenna [33] © 2010 IEEE.

3.7 Magneto-Electric Dipole Antennas

Researchers at the City University of Hong Kong have presented another interesting concept for mmWave applications; the magneto-electric dipole antenna. The antenna can be seen in Figure 3.13, where the planar top metal layer acts as an electric dipole while the vertical pins act as a quarter-wavelength patch. The antenna is fed through the middle feeding-pin that is connected to the T-shaped coupled strip. The structure might look quite complicated, but the authors claim that it is "a simple inherent architecture" [34] with low fabrication cost. The antenna achieved a very wide bandwidth, maximum gain of 7.5 dBi and a radiation pattern similar to a regular patch antenna (broadside radiation). It was modeled with the substrate Rogers RT Duroid 5880 with a permittivity of $\varepsilon_r = 2.2$.

Type [ref.]	Freq. (GHz)	Gain (dBi)	BW (GHz)	Rad. Eff. η_r
Magneto-electric dipole [34]	60	7.5	22	-

Table 3.5: Performance of the magneto-electric dipole antenna in [34]. BW denotes the -10 dB bandwidth.

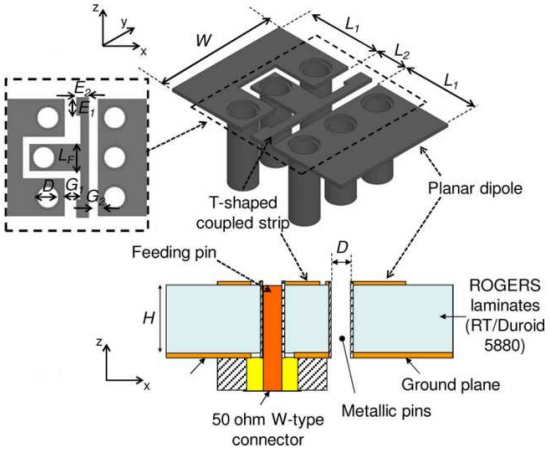

Figure 3.13: Electro-magnetic dipole antenna [34] © 2012 IEEE.

3.8 Conclusion

Based on what has been encountered in the literature study documented above, three different antenna designs were chosen to be modeled and evaluated for mobile station implementation. The chosen designs were:

I An aperture-coupled rectangular patch antenna.

II An aperture-coupled rectangular dielectric resonator antenna (DRA).

III An open-ended substrate integrated waveguide (SIW).

The choice of the patch and the DRA can be motivated by the extensive studies carried out concerning them, their similarities in performance and that their radiation pattern make it feasible to achieve a large coverage in the half sphere above the antenna. Both elements are small in size and realizable through low-cost fabrication processes due to their simple design. Moreover, for comparison in footprint size both the patch and the DRA will be designed as rectangular elements.

The aperture-coupling is recurring in the encountered research articles, and since a lot of concerns regarding mmWave antennas are connected to the integration of the circuit as a whole system, a feeding technique that isolates the radiating element can be advantageous as mutual coupling to other components can be reduced. This motivates the choice of feed to be aperture-coupling.

The SIW technique is a quite novel low-cost technique that have gained a lot of interest recently. A configuration of open-ended SIWs similar to the one in [33] could, if placed on the edges of the mobile station, possibly obtain a large coverage by placing the arrays on different edges. Due to the spatial limitations in a mobile station the horn will be excluded from the design as the antenna element will be too big. The antenna will be fed through a probe just as in [33] .

Rogers RT Duroid 5880 ($\varepsilon_r = 2.2$) can be seen to be a recurring material in related articles, which motivates the choice of this substrate for future simulations.

Regarding the material for the DRA, the substrate Rogers RT Duroid 6010 ($\varepsilon_r = 10.2$) is chosen for future modeling, as it is used in many of the related articles. Since copper is widely used for commercial applications, all metal will be modeled as such.

Comment

The article [8] is recommended for a thorough overview regarding mmWave communication systems and circuits, where a lot of reported results from AoCs and AiPs are listed. The antenna section is mostly focused on printed antenna results, with some DRAs occurring. The article [2] provides a good overview of different array solutions for mmWave antennas. The authors, Y. P. Zhang and D. Liu, have made a lot of work in the region of printed antennas for mmWave applications, and their work is recommended for further reading. The authors of [30] have published a lot of work within the region of SIW antennas and particularly BFNs. A good overview of their work can be found in [28]. Moreover, the article [35] considers design principles, loss mechanisms and transitions for both passive and active circuits developed through SIW technology.

Chapter 4

Selected Antenna Types

Based on the study presented in the Chapter 3, three different antenna designs were chosen for modeling and further evaluation. The underlying theory, characteristics and design approach of these three antenna concepts will therefore be presented here on a more profound level.

4.1 Patch Antennas

4.1.1 Geometry and Main Characteristics

A patch antenna consists of a dielectric substrate in between a metallic patch on top, and a ground plane below. The patches are typically rectangular or circular and the thickness h is much smaller than the wavelength ($h \ll \lambda$). A typical rectangular patch antenna is shown in Figure 4.1. There exist several ways of feeding this kind of structure, such as coaxial probe feed, microstrip feed and aperture-coupled feed. These will not be described in detail, and the analysis will be restricted to the choice of feeding technique for the upcoming simulations.

There exist more than one model explaining the operation principles of patch antennas, and one of the most popular ones are the cavity model. The following design formulas can be found in [36], where also the underlying theory regarding microstrip patch antennas are thoroughly described. Using the cavity model, the principle of operation is based on creating a resonant cavity for the electric field between the two metal pads ($\hat{\boldsymbol{z}}$-direction). By assuming that the metal patch and ground are perfect electric conductors (PEC), thus forcing the tangential electric field to be zero, the E-field distribution can be expressed as:

$$E_z(x) = -E_0 \sin(\frac{\pi x}{L}) \ , \ \ |x| \leq L/2 \tag{4.1.1}$$

The field is essentially constant along the width ($\hat{\boldsymbol{y}}$-direction) and varies along the length according to (4.1.1). The patch is thus resonant when the length is approximately half a wavelength in the substrate. However, as seen in Figure 4.1 the electric field fringes at the edges, making a more accurate approximation to be:

$$L_\mathrm{e} = L + 2\Delta L = \frac{\lambda_0}{2\sqrt{\varepsilon_\mathrm{r}}} \tag{4.1.2}$$

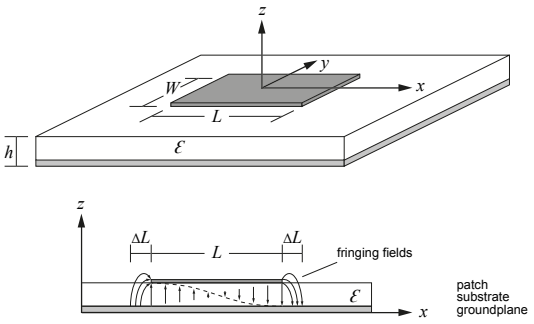

Figure 4.1: A patch antenna with top metal layer, a ground plane and dielectric substrate in between. In the lower figure, the electric field with the fringing field components are visible. Based on Figure 18.6.1 in [5].

where ΔL is the length extension, λ_0 is the free-space wavelength and ε_r is the dielectric constant of the substrate. The width is typically held between $L \leq W \leq 1.5L$ to suppress higher order modes while maintaining good bandwidth. The radiation characteristics from a patch antenna can be derived from the magnetic currents $\boldsymbol{J}_\mathrm{m} = -\hat{\boldsymbol{n}} \times \boldsymbol{E}$. In a similar way to electric currents, magnetic currents can be fourier transformed to obtain the radiating field. From the expression of $\boldsymbol{J}_\mathrm{m}$, one can see that the radiation is focused on the edges occurring at $x = \pm L/2$, where $\boldsymbol{J}_\mathrm{m} = -\hat{\boldsymbol{y}} E_0$ ($\hat{\boldsymbol{n}} = \pm\hat{\boldsymbol{x}}$ and $\boldsymbol{E} = \mp\hat{\boldsymbol{z}} E_0$). The contribution from the edges at $y = \pm W/2$ is quite small, which can be seen as the electric field is shifted symmetrical regarding the mid-line $x = 0$. This is visible in Figure 4.2.

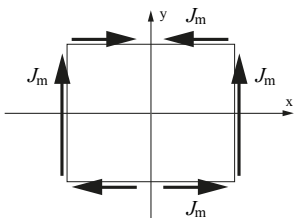

Figure 4.2: Magnetic currents along the boundaries of the patch. Along the lower and upper side respectively, the contribution from the magnetic currents can be seen as negliable.

Using image theory to replace the ground plane with equivalent currents, one can obtain the radiation vector $\boldsymbol{F}(\theta, \phi)$ through (2.1.1) by solving for $\boldsymbol{J}_\mathrm{m}$ over

$-W/2 \leq y \leq W/2$ and $-h \leq z \leq h$:

$$\boldsymbol{F}(\theta, \phi) = \iint \boldsymbol{J}_{\mathrm{m}}(\boldsymbol{r}') e^{\mathrm{j}k\hat{\boldsymbol{r}}\cdot\boldsymbol{r}'} \, \mathrm{d}y' \, \mathrm{d}z' \tag{4.1.3}$$

The radiation intensity and total radiated power can then be found through (2.1.4) and (2.1.5). The radiation pattern is shown in Figure 4.3, which shows a maximum radiation in the normal direction.

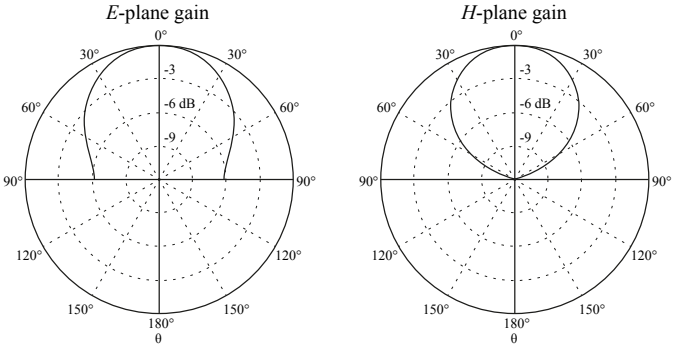

Figure 4.3: Normalized gain of a patch antenna in the E-plane ($\phi = 0$) and H-plane ($\phi = \pi/2$) respectively. Based on Figure 18.6.3 in [5].

Apart from the broadside radiation, another characteristic of patch antennas is the narrow bandwidth. The effect on choice of parameters and substrate will be introduced below.

4.1.2 Efficiency and bandwidth

For dielectric thicknesses $h \geq 0.02\lambda_0$ the conductive losses are quite suppressed leaving the main power loss due to surface waves. However as h is further increased, the power lost through surface waves also increases (see Section 2.9). This is undesirable, and the best radiation efficiency η_{r} is usually obtained with $h \simeq 0.02\lambda_0$ [37]. This applies for structures using dielectric material with relatively low permittivity. Using low permittivity substrates also enhances the bandwidth. Similarly, increasing the width W and height h can also be seen to improve the bandwidth. These aspects can be important to consider as the bandwidths of patch antennas are generally quite narrow.

4.1.3 Design

Usually the design approach uses the discussed theory above for a good approximation of initial parameters. By starting from the desired center frequency f_0, height of substrate material h and dielectric constant ε_{r} one determines the width W and length L through a series of steps. The W/L-ratio is usually between

$1 \leq W/L \leq 1.5$ for reasons discussed above, however as starting point this fraction might be considered through:

$$W = \frac{\lambda_0}{2}\sqrt{\frac{2}{\varepsilon_\mathrm{r}+1}} \tag{4.1.4}$$

Once the width is known, the effective dielectric constant can be decided:

$$\varepsilon_\mathrm{eff} = \frac{\varepsilon_\mathrm{r}+1}{2} + \frac{\varepsilon_\mathrm{r}-1}{2}\left[1+12\frac{h}{W}\right]^{-1/2} \tag{4.1.5}$$

To take into account the effect of the fringing fields occuring at the radiating edges ($x = \pm L/2$), the extension length of the patch needs consideration. An approximate relation is given in [36]:

$$\frac{\Delta L}{h} = 0.412\frac{(\varepsilon_\mathrm{eff}+0.3)\left(\frac{W}{h}+0.264\right)}{(\varepsilon_\mathrm{eff}-0.258)\left(\frac{W}{h}+0.8\right)} \tag{4.1.6}$$

where ΔL is the extension length. The effective length is now given as $L_\mathrm{e} = L + 2\Delta L$, making it possible to arrive at a value for the real length L:

$$L = L_e - 2\Delta L = \frac{\lambda_0}{2\sqrt{\varepsilon_\mathrm{eff}}} - 2\Delta L \tag{4.1.7}$$

With this said, it is still important to be aware of that an optimal design must be done through simulations and parametric changes simultaneously. The theory and design approach above gives a good overview on how to start and how to change parameters to get the desired performance, but small changes must always be done within the simulation software and eventually also in the fabricated design.

4.2 Dielectric Resonator Antennas

4.2.1 Geometry and Main Characteristics

A dielectric resonator antenna (DRA) is based on creating a resonant cavity of dielectric material with high permittivity. The high contrast of permittivity at the substrate-air interface causes constructive interference within the resonator thus forming a standing wave. The radiation is due to the leaked power from the DRA. The conventional designs of DRAs are hemispherical, cylindrical and rectangular. Compared to a hemispherical or cylindrical shape, a rectangular is relatively easy to fabricate and offers extra degrees of freedom as the height, width and length of the DRA need to be taken into consideration. Furthermore, a rectangular DRA offers a good comparison with a rectangular patch in terms of footprint. Therefore, the presented theory will be that of the rectangular DRA, which will also further be designed. A typical rectangular DRA is shown in Figure 4.4. The resonator is usually placed on a ground plane (Figure 4.5) and can be fed through varying feed mechanisms such as probe feed, aperture-coupled feed or direct microstrip feed. The analysis of these feeding techniques will be restricted to the choice which was used in the upcoming part of the thesis.

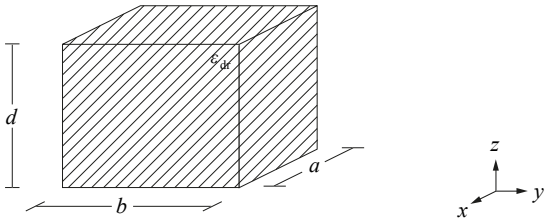

Figure 4.4: A rectangular dielectric resonator antenna.

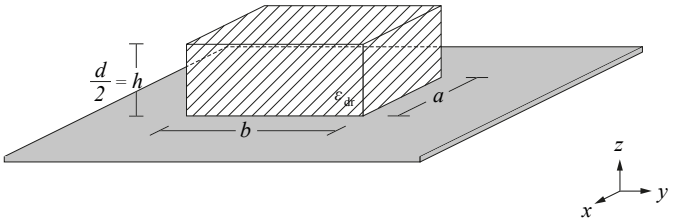

Figure 4.5: A rectangular dielectric resonator antenna mounted on a ground plane.

Making the assumption that the dielectric resonator of interest is of *very high* permittivity, the modes have been shown to satisfy specific boundary conditions [38, 39]. A rectangular DRA only supports nonconfined modes [40] leading to the following condition:

$$\boldsymbol{E} \cdot \hat{\boldsymbol{n}} = 0 \tag{4.2.1}$$

The lowest order modes are labeled as the TE^x_{111}-, TE^y_{111}- and TE^z_{111}-modes, and the resonant frequency can be found through the field components using the above stated boundary condition. E.g, consider a rectangular DRA with dimensions $|x| \leq a/2$, $|y| \leq b/2$ and $|z| \leq d/2$ and dielectric constant ε_{dr}, as shown in Figure 4.4. For the TE^y_{111}-mode, the electric field intensity components can be found through the magnetic potential to be [40]:

$$\begin{cases} E_x = -Ak_z \cos(k_x x) \sin(k_z z) \cos(k_y y) \\ E_y = 0 \\ E_z = -Ak_x \sin(k_x x) \cos(k_y y) \cos(k_z z) \end{cases} \tag{4.2.2}$$

Where k_i denotes the wavenumber along the i-direction inside the DRA and A is an arbitrary constant. The condition (4.2.1) leads to the following expression for the wavenumbers k_x and k_z:

$$k_x = \frac{\pi}{a} \quad , \quad k_z = \frac{\pi}{d} \tag{4.2.3}$$

Furthermore, using the dielectric waveguide model [26], k_y can be found through:

$$k_y \tan(\frac{k_y b}{2}) = \sqrt{(\varepsilon_{\mathrm{dr}} - 1)k_0^2 - k_y^2} \tag{4.2.4}$$

The resonant frequency is the one that have the above stated wavenumbers k_x and k_z, while k_y satisfies both (4.2.4) and

$$k_x^2 + k_y^2 + k_z^2 = \varepsilon_{\mathrm{dr}} k_0^2 \tag{4.2.5}$$

where k_0 is the wavenumber in free space, from which the frequency can be obtained through $k_0 = \dfrac{2\pi f_0}{c}$, with c being the speed of light in vacuum. This indicates that different dimensions can be employed to design a DRA at a specific frequency. This is important from the perspective of using rectangular DRAs in mobile stations. Their three dimensional profile obviously accounts for as a drawback compared to printed antennas, but the fact that the design is relatively flexible, one can still construct DRAs with larger footprints and lower heights. For practical purposes such as establishing a good feed to the DRA, they are usually mounted on top of a metallic ground plane which acts as an electric wall. The fields and resonant frequencies are then maintained if the length vertical to the ground (in this case d) is cut by half, i.e. $h = d/2$. This can be seen in Figure 4.4 and 4.5. The field distribution for the TE^y_{111}-mode is shown in Figure 4.6.

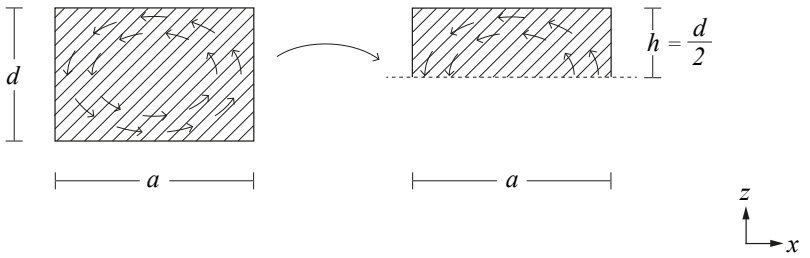

Figure 4.6: An approximate visualization of the TE^y_{111}-mode for a high permittivity DRA. To the left without ground plane, and to the right mounted on a ground plane.

A rectangular DRA radiates like a horizontal magnetic dipole, thus its pattern is similar to the one from a patch antenna. DRAs have been shown to have high radiation efficiencies at high frequencies, mostly due to that other losses than radiation are restricted to those in the dielectric [41]. Moreover, the bandwidths are usually greater than for patch antennas. It can, by just as above assuming *very high* permittivity, be derived an analytical relation [40] between the radiation Q factor Q_{rad} and the permittivity stating that

$$Q_{\mathrm{rad}} \propto (\varepsilon_{\mathrm{dr}})^{3/2}$$

This is not entirely correct as the value of the dielectric constant decreases, but nevertheless shows that the radiated power P_{rad} is increased (2.7.1), and the bandwidth can be kept higher by using low permittivity substrates (2.4.5). In related

articles [25–27], the used substrates have a permittivity of $\varepsilon_{\mathrm{dr}} \sim 10$, and these antennas obtained high radiation efficiencies, percentage bandwidths of around $3 - 6\,\%$ and gain values of the same magnitude as patch antennas.

4.2.2 Design

For designing a rectangular DRA mounted on a ground plane, a good first step is to follow the derivation of the resonant frequency given in (4.2.3) - (4.2.5). For a given frequency, one can then obtain the dimensions a, b and $h = d/2$. Note however that these formulas are based on the assumption that the permittivity of the substrate is very high (approaching infinity), and doesn't apply straight forward to a choice of lower permittivity substrate. The field distribution however is similar. For obtaining a final design, it is reasonable to validate the field inside the DRA by checking that the desired mode is excited, while optimizing the design parameters.

4.3 Substrate Integrated Waveguide Antennas

4.3.1 Geometry, Design and Main Characteristics

A substrate integrated waveguide (SIW) consists of a dielectric substrate in between two horizontal top- and bottom metallic covers. By introducing two vertical rows of metal via holes the waveguide is created. A top view of a SIW is shown in Figure 4.7. The structures are relatively simple to fabricate using low-cost PCB technology, making them recurring as proposed antennas for millimeter wave applications. It is noticeable that most of the encountered designs use slots in the top metal plane to enable radiation, however for the design used in this thesis this is not the case. Instead it radiates from aperture, the open end of the waveguide. Therefore, this theory part explains the underlying principles of regular waveguides and how they are transformed for designing SIWs. SIWs can also be fed through numerous feeding techniques. In this thesis, the SIW will be probe-fed with a back wall introduced for constructive interference.

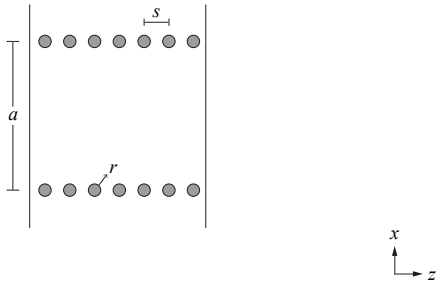

Figure 4.7: Top view of a substrate integrated waveguide. a is the width, s the via spacing and r the via radius.

Starting from a rectangular waveguide of four conducting metal walls filled

with air, the dominant mode is occurring at the lowest cutoff frequency. For a waveguide with width a bigger than the height b, this happens when the width a is equal to half a wavelength as in Figure 4.8, thus leading to the following relations:

$$\lambda_{\mathrm{co}} = 2a \;\; ; \;\; k_{\mathrm{co}} = \frac{\pi}{a} \;\; ; \;\; f_{\mathrm{co}} = \frac{c}{2a} \tag{4.3.1}$$

If the height $b \leq a/2$ the second cutoff frequency will occur for a mode along the width as well, i.e. $f_{\mathrm{co2}} = 2f_{\mathrm{co}}$. For single mode operation the frequency should be chosen appropriately according to these two cutoff frequencies. A usual approach is thus to choose $f_0 = 1.5f_{\mathrm{co}}$. A simple approach of design can then be made as follows. E.g, if $f_0 = 28\,\mathrm{GHz}$, then the cutoff frequency for the TE_{10}-mode is $f_{\mathrm{co}} = f_0/1.5 = 18.6\,\mathrm{GHz}$. The width a can then be estimated to $a = \mathrm{c}/2f_{\mathrm{co}}$, where c as usual is the speed of light in vacuum. Based on the assumptions above, the height b should then be $b \leq a/2$. When introducing a substrate instead of air, the final step is just to scale all dimensions with $1/\sqrt{\varepsilon_{\mathrm{r}}}$.

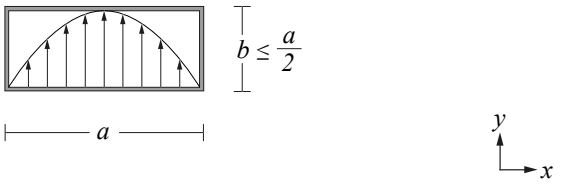

Figure 4.8: The TE_{10}-mode along the width a of a rectangular waveguide.

The translation from a regular rectangular waveguide to a substrate integrated one, whose geometrical properties is shown in Figure 4.7, are relatively simple from a theoretical point of view. Due to their similarity, a geometrical translation can be done quite easily while maintaining similar field characteristics. Empirical equations have been obtained [35, 42], for which this has been proven to hold. For a waveguide width of a_{eff}, the SIW width a can be obtained through:

$$\begin{aligned} a_{\mathrm{eff}} &= a - 1.08\frac{(2r)^2}{s} + 0.1\frac{(2r)^2}{a} \\ a &= \frac{2a_{\mathrm{eff}}}{\pi}\cot^{-1}\left(\frac{\pi s}{4a_{\mathrm{eff}}}\ln\frac{s}{4r}\right) \end{aligned} \tag{4.3.2}$$

where s is via spacing and r is the via radius. As long as the spacing s between the vias is kept relatively small compared to the radius r, the radiation leakage at the sidewalls can be neglected. The smaller the spacing and bigger the radius, the more the sidewalls approaches continuous metal. The s/r-ratio should be no more than $s/r \leq 4$ recommended [35].

By choosing the width a as mentioned, only modes of the lowest order are ensured to propagate in the waveguide. When introducing the back wall, the antenna becomes relatively narrow in bandwidth performance since the interference is only constructive for the frequency that the waveguide is designed for. The three

major loss mechanisms in a SIW are the dielectric losses, the conductor losses and the radiation leakage losses. The dielectric losses only depends on the chosen substrate, and the radiation losses can be held to a minimum by appropriate dimensions of the side wall vias as explained above. The conductor losses however, restricts the choice of substrate thickness, or height b, as these losses are inversely proportional to b [35]. Thus, in order to lower conductor losses, the height needs to be large enough, limiting how "flat" the structure can be made. For the SIW design a probe feed is used to excite the desired mode. A probe consists of an inner cylinder which stretches into the substrate with an appropriate length. An outer cylinder is connected to ground, with substrate in between the two cylinders, and the impedance is matched for the desired frequency by adjusting the length of the inner probe. The placement of the probe also has an impact on the matching. The distance from the probe-feed to the back wall should be approximately $\lambda_{\varepsilon_r}/4$ for constructive interference of the reflected wave.

An open-ended waveguide radiates like an aperture antenna, where the fields at the opening determines the radiation vector. The magnetic currents $\boldsymbol{J}_m$ can be obtained through $\hat{\boldsymbol{n}} \times \boldsymbol{E}$, and the radiation intensity $U(\theta, \phi)$ can then be found through (2.1.1) and (2.1.4). The radiation pattern is narrow in the H-plane (parallel to the width a) and broad in the E-plane (parallel to the height b).

4.4 Aperture-coupling

An aperture-coupling consists of a transmission line placed on the bottom of a substrate, on which a ground plane is placed on top. The ground plane is then cut open, leaving a slot opening that couples to the antenna placed on the top. For a patch antenna an additional substrate is placed above the ground plane before introducing the antenna, while for a DRA the dielectric block is placed directly on top of the ground plane. The concept can be visualized in Figure 4.9. There exists numerous shapes of the introduced slot, but for simplicity the introduction will be restricted to the standard rectangular slot. The advantages of such a feed is the isolation between radiating element and feed network caused by the intervening ground plane, and the fact that the antenna and the feed network can be optimized independently. The principle of the coupling is based on the energy from the transmission line being coupled to the antenna through the slot. The electric field between the transmission line and the ground plane can be replaced by equivalent magnetic currents $\boldsymbol{J}_m$ within the slot. The magnetic current then couples to the magnetic field intensity $\boldsymbol{H}$ in the above lying structure. Hence, the slot should be placed at a location were the magnetic field is strong in the antenna structure for good magnetic coupling. For both the patch and the DRA this occurs in the center line of the structure. Several new degrees of freedom arise when introducing this kind of feed; the dimensions of the slot L_{ap}, W_{ap}, the stub length of the transmission line L_s and the thickness of the substrate h. All these are visible in Figure 4.9. There are no direct design approaches for combining an aperture-coupling with a specific choice of antenna element, but the optimization of the feed needs to be validated through checking that the appropriate antenna operation is obtained. Consistent analysis have been carried out in several cases

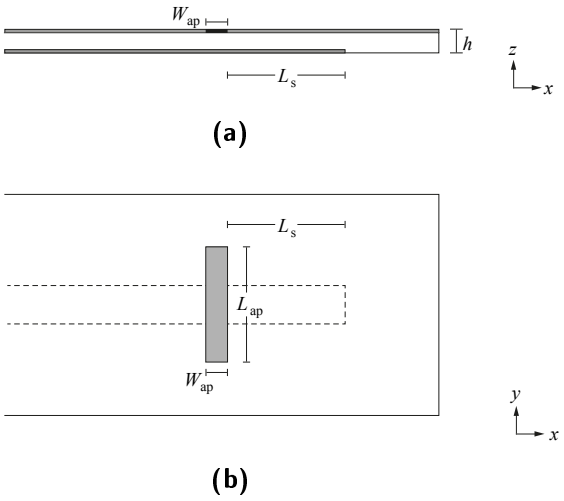

Figure 4.9: Aperture-coupling through a rectangular slot. (a) cross section in xz-plane, (b) cross section in xy-plane.

connected to patches [6, 43] and DRAs [44] which can leverage insight in the design approach. In [6] the use of the transmission line model and the modal expansion model shows how the three components (the patch, the aperture and the microstrip line) are linked together regarding the impedance, and how they should be tuned to get good matching.

The slot length is the major parameter for tuning. The slot should be electrically small, meaning that it is not self-resonant. To enable good coupling however, the slot length L_{ap} still needs to be sufficiently large, a too small slot length results in undercoupling. Moreover, the slot dimensions affect the resonant frequency of the antenna element [6]. Increasing L_{ap} increases the resonance resistance R_{res} which decreases the resonance frequency f_{res} and vice versa. The open-circuit stub length L_{s} should be approximately $\lambda_{\varepsilon_{\mathrm{r}}}/4$ to enable strong coupling. Minor tuning can also be achieved by changing the stub length, were the impedance change according to $-jZ_{0\mathrm{ms}}\cot(\beta_{\mathrm{ms}}L_{\mathrm{s}})$, where $Z_{0\mathrm{ms}}$ is the characteristic impedance and β_{ms} is the propagation constant of the transmission line [6].

Chapter 5
Single Element Performance

To confirm that the performance characteristics of the proposed designs are consistent with the theory, simulations were performed for a single element approach regarding all three antenna types; the patch, the dielectric resonator (DRA) and the substrate integrated waveguide (SIW).

5.1 Simulation Software

The simulation software used is Computer Simulation Technology (CST) MICROWAVE STUDIO, where also all designs are modeled. The software offers usage of several kinds of solvers, e.g. the time domain solver and the frequency domain solver, that each have their respective advantages. To validate that obtained results are accurate, it can also be good to do a resolution check.

5.2 Resolution and Solver

A resolution test was done on the return loss, and the results are visible in Figure 5.1. It can be seen that the return loss is quite stable, with a slight shift in center frequency for the patch and SIW. This can be considered to be negligible since the final performance needs to be evaluated through measurements. Thus, frequency shifts will appear in later stages anyway. The time domain solver will be used for future simulations, as it is significantly faster than the frequency domain solver. The frequency solver uses tetrahedral (four triangular faces) mesh cells, while the time domain solver uses three dimensional rectangular hexahedral (six faces) mesh cells, which are suitable for designs built up by rectangular blocks. A resolution of 40 steps per wavelength will be chosen for the patch and DRA, while 50 steps per wavelength is chosen for the SIW to get a slight better refinement of the circular vias.

5.3 Designs and performances

The finalized single element designs are an aperture-coupled patch antenna, an aperture-coupled DRA and a probe-fed SIW. All designs are scaled for operating at both 15 GHz and 28 GHz. All metal is modeled as copper (Cu) with electric

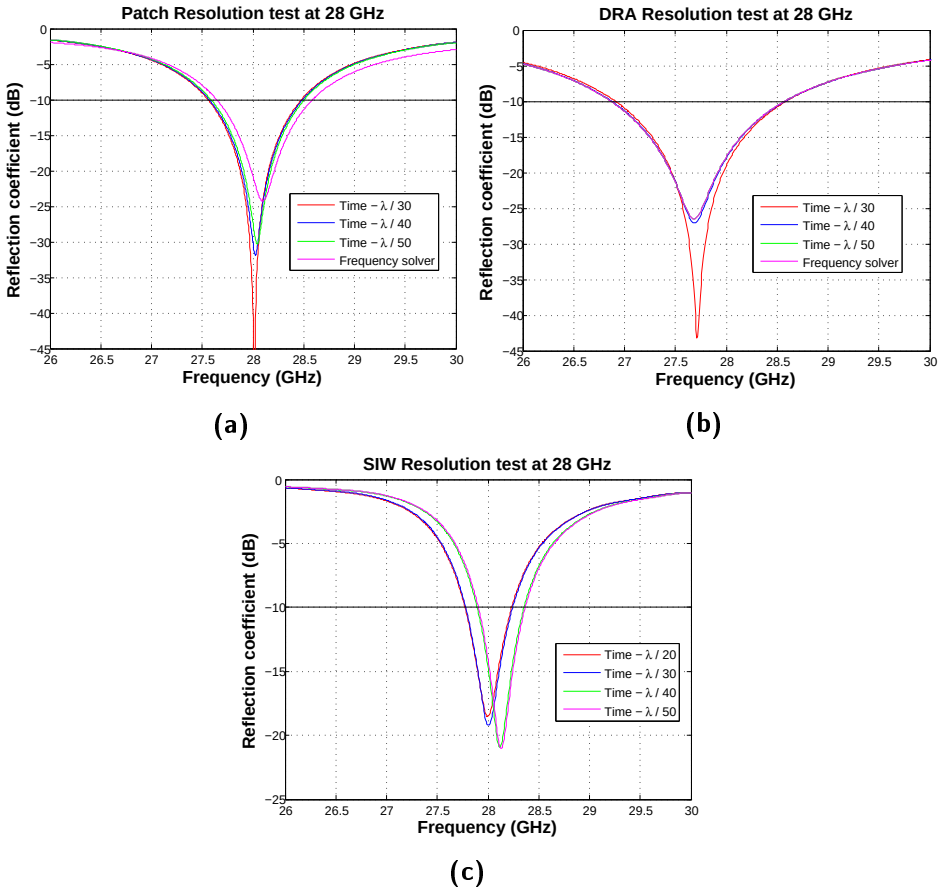

Figure 5.1: Resolution test performed for, (a) patch, (b) DRA and (c) SIW. Time domain - Hexahedral mesh, Frequency domain - Tetrahedral mesh.

conductivity $\sigma = 5.8 \cdot 10^7\,\mathrm{S/m}$, while the different substrates used are presented below. For comparison, all models at respective operation frequency have been implemented with the same finite sized ground plane. The size of the ground plane has an impact on the obtained return loss and radiation pattern, so for the sake of obtaining simulation results that are truly comparable with realistic measurements this has to be given significantly more attention. However, for the first step to obtain well functioning designs for comparison with one another, a chosen size has been selected and used. The transmission line for the aperture-coupling, and the probe for the probe feed are both designed to obtain a reference impedance Z_0 of $50\,\Omega$ respectively.

5.3.1 Aperture-coupled patch

The design approach of the aperture-coupled patch antenna is primarily based on what was discussed in Section 4.1.3, with a suitable size of the slot. The substrate is Rogers Duroid RT 5880 and is modeled in CST with $\varepsilon_\mathrm{r} = 2.2$ and $\tan\delta = 0.0009$ at $f = 8 - 40\,\mathrm{GHz}$. Two cross sectional views of the design are visible in Figure 5.2, where all fundamental parameters are noted.

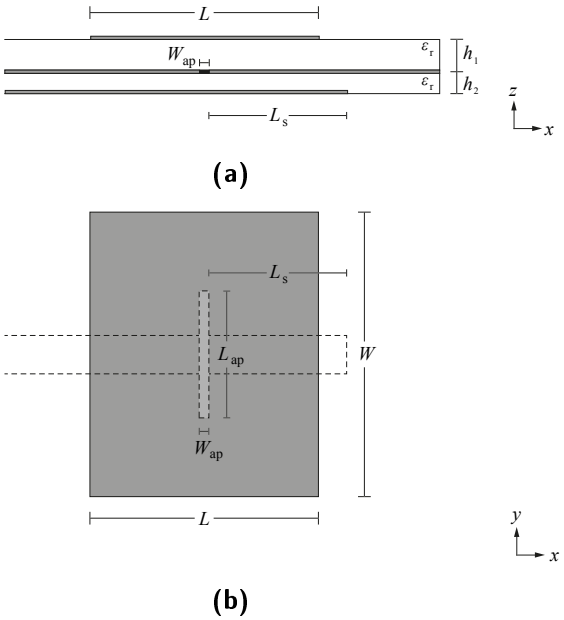

Figure 5.2: Design of the aperture-coupled patch antenna. (a) cross section in xz-plane, (b) cross section in xy-plane.

The size of the actual patch is chosen such that $L \sim \lambda_{\varepsilon_\mathrm{r}}/2$ and $1 \leq W/L \leq 1.5$. The substrate wavelength is $\lambda_{\varepsilon_\mathrm{r}} = \lambda_0/\sqrt{\varepsilon_\mathrm{r}}$, thus for 28 GHz with chosen substrate it is 7.22 mm and for 15 GHz it is 13.5 mm. In Table 5.1 it can be seen that the resonant length is $L = 0.43\lambda_{\varepsilon_\mathrm{r}}$, hence a bit smaller than half a wavelength. The substrate thicknesses h_1 and h_2 were chosen in order to achieve low losses, referring to what was said in Section 4.1. Available thicknesses can be found on Rogers website [23]. The top substrate thickness h_1 is approximately $0.02\lambda_0$.

The aperture-coupling was designed in order to get good coupling, referring to Section 4.4. However, since there are no direct rules of design, good ratios of the different parameters were used from [6] and [43], scaled according to desired operating frequency and finally optimized in CST. The stub length L_s is approximately a quarter wavelength in the substrate. The final dimensions of the constructed patch antennas are shown in Table 5.1, with all lengths in mm. The thickness of the copper is $18\,\mu$m.

The results obtained from the simulations are consistent with theory. The radiation pattern are shown in Figure 5.3 in both the E-plane ($\phi = 0$) and the

	Frequency	
Dim. (mm)	15 GHz	28 GHz
L	5.8	3.175
W	7.2	4.05
h_1	0.508	0.254
h_2	0.305	0.127
L_{ap}	3.15	1.58
W_{ap}	0.225	0.12
L_{s}	3.21	1.75

Table 5.1: Dimensions of constructed patch antennas for 15 GHz and 28 GHz, according to Figure 5.2. All lengths are in mm.

H-plane ($\phi = \pi/2$) for the patch at 28 GHz. Similar patterns were obtained for 15 GHz. It can be seen that the pattern strongly resembles the radiation pattern in Figure 4.3, however some backside radiation occurs due to the slot in the ground plane. The beam is relatively broad with half power beamwidths (HPBW) of 77° (xz) and 74° (yz). The maximum gain for both antennas are 7.5 dBi and 7.4 dBi at 15 GHz and 28 GHz respectively, and the percentage bandwidths are $\sim 3\,\%$, exceeding 500 MHz for both 15 GHz and 28 GHz. The results are listed in Table 5.4 and 5.5, and the reflection coefficients are depicted in Figure 5.9a and 5.9b.

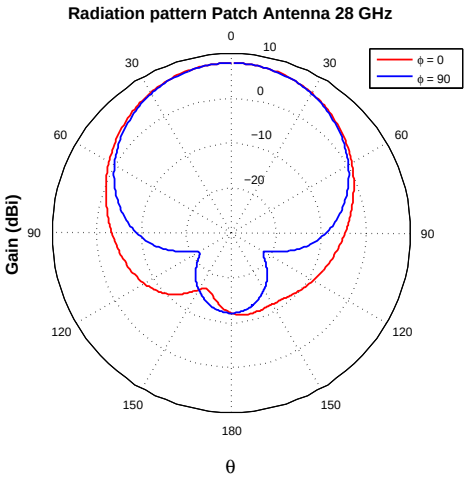

Figure 5.3: Simulated radiation pattern for the single patch antenna at 28 GHz.

5.3.2 Aperture-coupled DRA

Just as with the patch, the substrate is modeled in CST using Rogers Duroid RT 5880 with $\varepsilon_{\mathrm{r}} = 2.2$ and $\tan\delta = 0.0009$ at $f = 8 - 40$ GHz. The substrate

for the dielectric resonator is chosen with respect to what has been encountered in literature, and is chosen to be Rogers RT 6880 with $\varepsilon_{\mathrm{dr}} = 10.2$ and $\tan\delta = 0.0023$. Two cross sectional views of the designs are visible in Figure 5.4, where all parameters are noted.

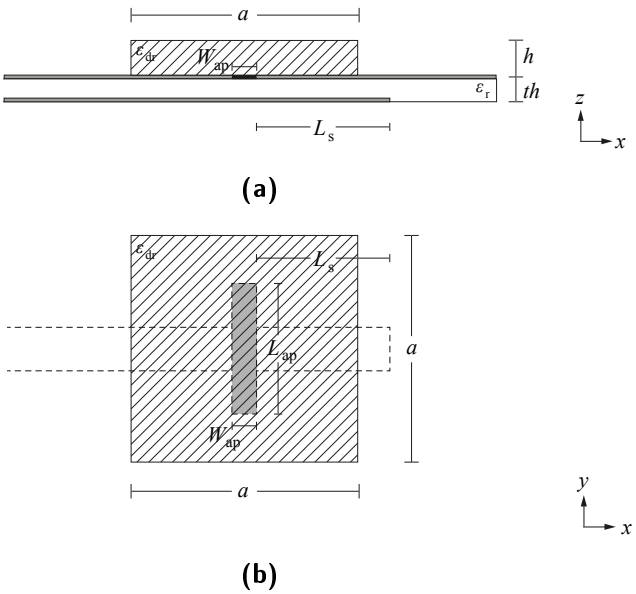

Figure 5.4: Design of the aperture-coupled DRA antenna. (a) cross section in xz-plane, (b) cross section in xy-plane.

The theory presented in section 4.2 and 4.4 was used to get a primary base for the design of the DRA and the aperture-coupling respectively. Furthermore, reference articles [40, 44] were helpful in order to obtain good dimension ratios for good coupling through the aperture. The dielectric resonator has a quadratic surface of size a^2 with height h. Since the slot is cut in the y-direction, the TE^{y}_{111}-mode is excited. The final dimensions of the constructed DRA antennas are shown in Table 5.2, with all lengths in mm. The thickness of the copper is 18 μm.

The obtained results can be seen as consistent with theory. The bandwidth is wider than for the patch, with a similar radiation pattern. It is shown in Figure 5.5 for 28 GHz in the E-plane ($\phi = 0$) and the H-plane ($\phi = \pi/2$). A broader beam is obtained than that for the patch, with HPBW_{xz} of 90° and HPBW_{yz} of 80°.

The maximum gain for both antennas are 6.5 dBi and 6.3 dBi at 15 GHz and 28 GHz respectively, and the percentage bandwidths are $\sim 6\,\%$, corresponding to 960 MHz at 15 GHz and 1660 MHz at 28 GHz. All the simulated results are listed in Table 5.4 and 5.5, and the reflection coefficients are depicted in Figure 5.9a and 5.9b.

	Frequency	
Dim. (mm)	15 GHz	28 GHz
a	4.3	2.3
h	2.5	1.34
th	0.305	0.305
L_{ap}	3.1	1.66
W_{ap}	0.58	0.31
L_{s}	4.3	2.3

Table 5.2: Dimensions of constructed DRAs for 15 GHz and 28 GHz, according to Figure 5.4. All lengths are in mm.

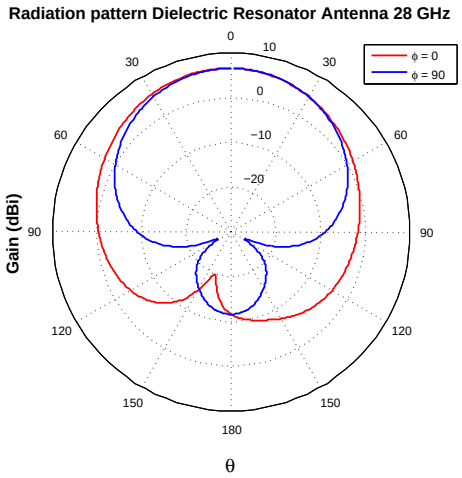

Figure 5.5: Simulated radiation pattern for the single DRA antenna at 28 GHz.

5.3.3 Probe-fed SIW

The design approach for the SIW is based on the theory presented in Section 4.3. The SIW consists of two parallel metal plates with dielectric substrate in between. The vertical walls are constructed by periodically placed metallic vias, and the antenna is fed by a probe. Two cross sectional views of the design are shown in Figure 5.6. All design parameters depicted in this figure are shown in Table 5.3 for the final design. The thickness of the copper is 210 μm.

The substrate material is modeled as AR25 with $\varepsilon_{\mathrm{r}} = 3.6$ and $\tan\delta = 0.0035$. Due to the large contrast in dielectric constant at the substrate-air interface, a good resonance is obtained if the length is approximately one wavelength in the substrate, i.e. in the 28 GHz-case $L \sim \lambda_{\varepsilon_{\mathrm{r}}} = 10.7/\sqrt{3.6} = 5.65$ mm. Good matching for desired operational frequency is obtained by appropriate probe length L_{p} and distance from the back wall L_{q}. The probe is placed approximately a quarter wavelength distance L_{q} from the back wall for constructive interference. Using the

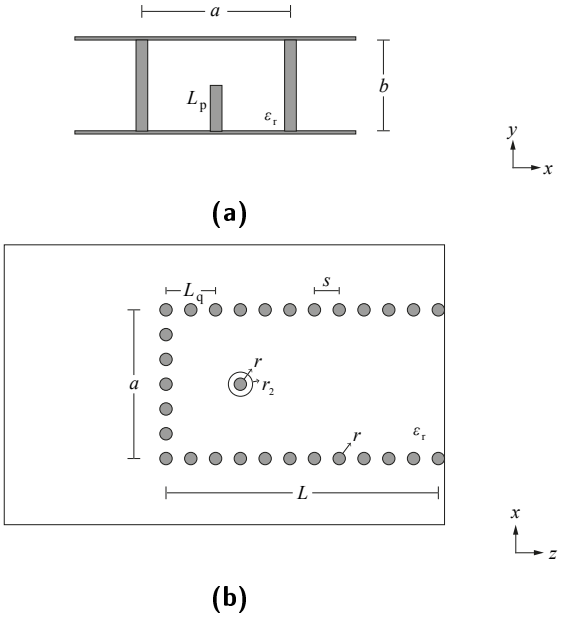

Figure 5.6: Design of the SIW antenna. (a) cross section in xy-plane, (b) cross section in xz-plane.

design approach of a rectangular waveguide [5], the design was primarily tried with vertical walls to confirm good performance. The effective width a_{eff} of the rectangular waveguide was then transformed into the width of the integrated waveguide a through (4.3.2). To reduce losses due to leakage between the vias, the spacing-to-radius ratio should be no bigger than $s/r \leq 4$.

	Frequency	
Dim. (mm)	15 GHz	28 GHz
a	8.6	4.6
h	3.7	2
L	9.86	5.8
L_q	3	1.42
L_p	1.27	0.56
s	0.58	0.58
r	0.22	0.22
r_2	0.5	0.5

Table 5.3: Dimensions of constructed SIW antennas for 15 GHz and 28 GHz, according to Figure 5.6. All lengths are in mm.

The results from the simulations show that the maximum radiation appears in the direction of the aperture. The radiation pattern is shown in Figure 5.7 in

the E-plane ($\phi = 0$) and the H-plane ($\phi = \pi/2$). The pattern might be somewhat more difficult to interpret than the two former designs, thus a three dimensional view is also shown in Figure 5.8.

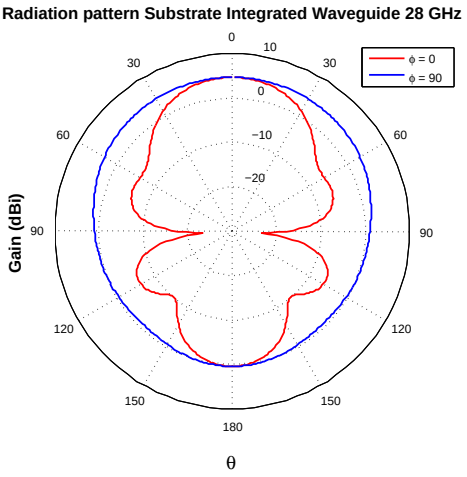

Figure 5.7: Simulated radiation pattern for the single SIW antenna at 28 GHz.

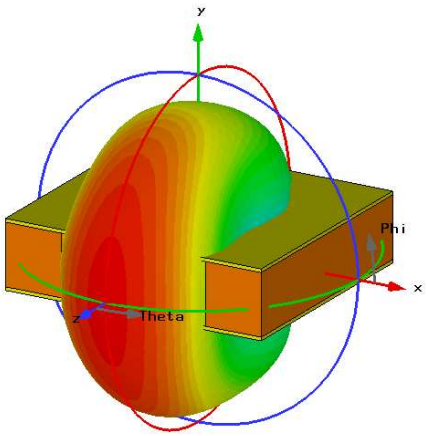

Figure 5.8: Simulated radiation pattern for the single SIW antenna at 28 GHz. Three dimensional view.

The simulated maximum gain is 4.3 dBi and 3.9 dBi at 15 GHz and 28 GHz respectively, with a narrow bandwidth of 2.3 % and 1.7 % - none of which exceeds 500 MHz. The quasi-omnidirectional radiation pattern gives a quite broad beam with a HPBW$_{yz}$ of 160°, while HPBW$_{xz}$ is quite narrow in comparison (56°). The reflection coefficient is depicted in Figure 5.9b.

5.4 Comparison

The single element performance of the three different designs have some quite distinguishable differences. The gathered results are listen in Table 5.4 and 5.5, and the return loss can be seen in Figure 5.9. The patch has the highest maximum gain, while the SIW has the lowest. All obtained bandwidths for the patch and the DRA exceeds 500 MHz in both bands, while the bandwidth of the SIW is very narrow, not exceeding 500 MHz in any of the two cases. The placement of the probe and the length of the SIW make the antenna very sensitive for the frequency range within which the antenna functions well, causing the narrow bandwidth (Section 4.3, p. 36).

All antenna designs achieved relatively high radiation efficiencies, with the SIW having the lowest one (85 %).

An important thing to point out is the difference in radiation pattern between the SIW and the patch and the DRA respectively. All three designs have been modeled with the z-axis pointing in the direction of maximum radiation. However, the two latter one have maximum radiation in broadside, while the SIW radiates in a planar direction.

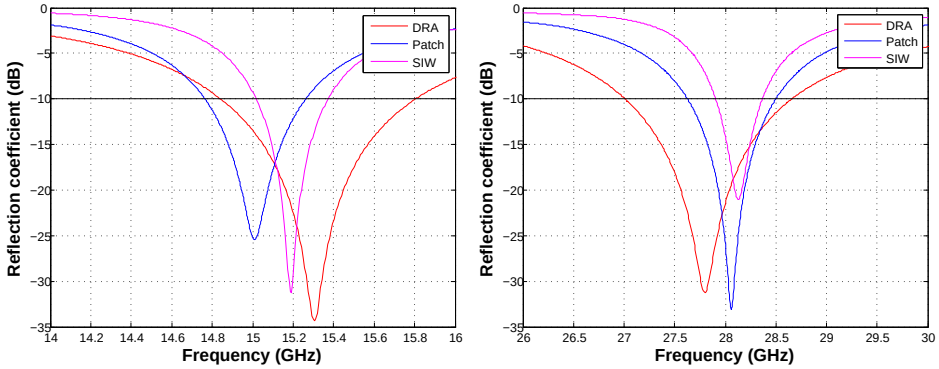

Figure 5.9: Reflection coefficients (dB) for antenna designs at (a) 15 GHz and at (b) 28 GHz.

15 GHz			
	Patch	DRA	SIW
Max. Gain (dBi)	7.5	6.5	4.3
BW (-10 dB)			
(MHz)	500	960	350
(%)	3.3	6.4	2.3
Rad. Eff. η_r	95 %	96 %	88 %
$\mathrm{HPBW}_{\mathrm{xz}}$ ($\phi = 0$)	76°	88°	63°
$\mathrm{HPBW}_{\mathrm{yz}}$ ($\phi = \pi/2$)	74°	78°	173°

Table 5.4: Summary of obtained results for all three single antenna designs at 15 GHz.

28 GHz			
	Patch	DRA	SIW
Max. Gain (dBi)	7.4	6.3	3.9
BW (-10 dB)			
(MHz)	890	1660	470
(%)	3.2	5.9	1.7
Rad. Eff. η_r	94 %	96 %	85 %
$\mathrm{HPBW}_{\mathrm{xz}}$ ($\phi = 0$)	77°	93°	56°
$\mathrm{HPBW}_{\mathrm{yz}}$ ($\phi = \pi/2$)	73°	79°	165°

Table 5.5: Summary of obtained results for all three single antenna designs at 28 GHz.

Chapter 6

Characterization of Phased Arrays in Mobile Terminal

In this chapter the motivation for usage of phased arrays in the mobile terminal is presented. Further, the novel characterization method of phased arrays using the coverage efficiency is described and in order to apply this, an estimated channel model is set up. As the 15 GHz band is less explored than the 28 GHz band, a focus is from here on held at 15 GHz as operational frequency.

6.1 Beamforming and Steering for mmWave Cellular Channel

The use of beamforming and steering can be explained by the additional losses arising when moving up to higher frequencies than those exploited in the cellular bands today. Between base station and mobile terminal, the propagation characteristics for a certain operation frequency can be explained by Friis' formula:

$$P_{\mathrm{R}} = \frac{P_{\mathrm{T}} G_{\mathrm{T}} G_{\mathrm{R}} \lambda^2}{(4\pi d)^2} \tag{6.1.1}$$

where P_{R} and G_{R} are received power and gain respectively, P_{T} and G_{T} are transfered power and gain respectively and d is the distance between the antennas. Neglecting all losses other than the free-space path loss L_{fs}, this can be recognized as:

$$L_{\mathrm{fs}} = \left(\frac{4\pi d}{\lambda}\right)^2 = \left(\frac{4\pi d f}{\mathrm{c}}\right)^2 \tag{6.1.2}$$

where c is the speed of light in vacuum. For a fixed distance d, it can be seen that the free-space path loss increases proportionally to the frequency squared. Moving from today's cellular bands (800 MHz − 2.6 GHz) up to 15 GHz, the additional free-space path loss needs to be taken into account. Increasing the mobile antenna gain is one way to compensate. Further, the effective aperture A_{eff} is a measure of how effective an antenna is at receiving power, and is related to the antenna's gain according to:

$$G = \frac{4\pi A_{\mathrm{eff}}}{\lambda^2} = 4\pi A_{\mathrm{eff}} \left(\frac{f}{c}\right)^2 \tag{6.1.3}$$

The physical aperture of the considered antenna elements decreases with the square of the wavelength, so the total physical aperture can be maintained, moving from 3 GHz to 15 GHz, by providing multiple antenna elements. In general, the relation between an antenna's physical aperture and its effective aperture is only directly related for antennas whith apertures large compared to the operational wavelength (e.g. parabolic reflectors). But nevertheless, it indicates that the same quantities of sent and received energy can be obtained using higher frequencies.

The use of an antenna array results in a higher gain and thereby also in a narrower beam. This indicates that it needs to be steerable in order to establish a good link between base station and mobile terminal in an arbitrary case. As explained in Section 2.10, the radiated beam can be made steerable through phased array systems. A typical scenario can be seen in Figure 6.1.

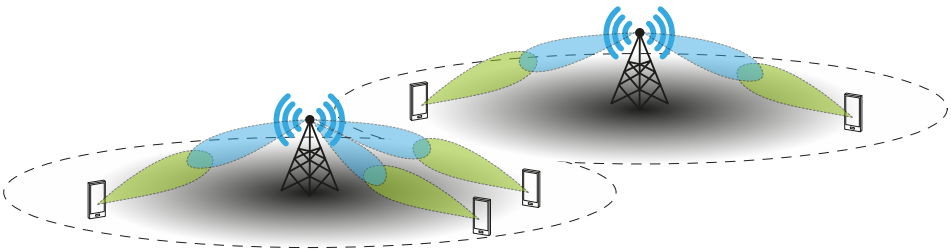

Figure 6.1: Beamforming and steering applied to achieve a good link in mmWave cellular communication.

For phased arrays, the phase shift between elements can be both fixed or arbitrary. Using fixed phase shifts, the steering of the radiated beam is much easier to control. Moreover, they are also easier to realize concerning hardware implementation and digital aspects than the arbitrary phase shift. Arbitrary phase shifts also result in unpredictable radiation patterns, which might not be of as much use concerning this topic, compared to a well-controlled, steerable narrow beam.

Employing phased arrays at the mobile terminal results in a separate radiation pattern for each fixed phase shift. The steerability is crucial to obtain optimal coverage since every phase shift exhibits a narrow high gain beam. It is thus fundamental to characterize such a system through the obtainable coverage from its total scan pattern, as illustrated in Figure 6.2.

The total scan pattern can be found from all radiation patterns corresponding to the different phase shift inputs, by extracting the best achievable gain at every angular distribution point (θ, ϕ). This can then be evaluated in terms of the coverage efficiency η_c with respect to a threshold level of the required gain.

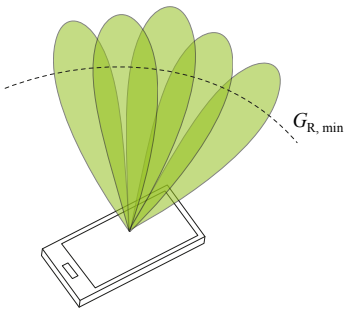

Figure 6.2: Phased array configurations characterized through the coverage of its total scan pattern.

6.2 Coverage Efficiency

The coverage efficiency η_{c} can be found as the ratio of achieved solid angle coverage for a given value of minimum gain $G_{\mathrm{R,min}}$, to all solid angles over a sphere:

$$\eta_{\mathrm{c}} = \frac{\text{Solid Angle Coverage}}{\text{Total Solid Angles}} = \frac{\Omega_{\mathrm{c}}}{\Omega_{\mathrm{Sph}}} \tag{6.2.1}$$

The total solid angle of a sphere is $\Omega_{\mathrm{Sph}} = 4\pi$. The solid angle coverage is found from all solid angles that meets the minimum gain requirement, i.e. the total solid angle where $G_{\mathrm{R}} \geq G_{\mathrm{R,min}}$.

6.3 Channel Model for 15 GHz Cellular

The threshold level of the required gain can be found by setting up a model for the link budget system, i.e. by accounting for all gains and losses between transmitter and receiver. Cellular communication in urban environments can be divided into either line-of-sight (LOS) or non-line-of-sight (NLOS) propagation. The ideal LOS scenario is described by Friis' formula in its simplest form (6.1.1), where only the free space path loss (6.1.2) is considered. By rewriting (6.1.1) into dB-scale and solve for received gain G_{R} one obtains:

$$G_{\mathrm{R}} = P_{\mathrm{R}} - P_{\mathrm{T}} - G_{\mathrm{T}} + 20\log\left(\frac{4\pi d}{\lambda}\right) \tag{6.3.1}$$

An ideal scenario is unfortunately almost never the case and there exist numerous additional loss mechanisms in a channel. Precipitation, atmospheric absorption, polarization mismatch and user's impact are all sources of extra losses. For NLOS conditions the channel is further complicated by blocking obstacles (shadowing), multipath propagation causing interference at the receiver (fading), signal refraction through buildings, reflections off building walls or ground one or multiple times. Thus, it is evident that a realistic channel model can be difficult to realize without empirical studies carried out.

However, the purpose of using high gain steerable antennas is to establish the optimum link in any scenario, and with cell sizes of 200 m, it is reasonable to assume that building-reflection paths will be one of the more common types of NLOS links. Additional losses in terms of polarization mismatch, precipitation, atmospheric absorption and building-reflection can then be added to the model according to:

$$G_{\mathrm{R}} = P_{\mathrm{R}} - P_{\mathrm{T}} - G_{\mathrm{T}} + 20\log\left(\frac{4\pi d}{\lambda}\right) + 20\log\left(\frac{1}{|\Gamma|}\right) + L_{\mathrm{m}} \tag{6.3.2}$$

where L_{m} is a general term including all above mentioned losses other than reflection losses, and Γ is the reflection coefficient for either transverse electric (TE) or magnetic (TM) incoming signals. These can be found through Fresnel's equations for reflection according to:

$$\begin{aligned} \Gamma_{\mathrm{TE}} &= \frac{\cos\theta_i - \sqrt{\varepsilon_{\mathrm{r}} - \sin^2\theta_i}}{\cos\theta_i + \sqrt{\varepsilon_{\mathrm{r}} - \sin^2\theta_i}} \\ \Gamma_{\mathrm{TM}} &= \frac{\varepsilon_{\mathrm{r}}\cos\theta_i - \sqrt{\varepsilon_{\mathrm{r}} - \sin^2\theta_i}}{\varepsilon_{\mathrm{r}}\cos\theta_i + \sqrt{\varepsilon_{\mathrm{r}} - \sin^2\theta_i}} \end{aligned} \tag{6.3.3}$$

where θ_{i} is the incident angle according to Figure 6.3. A TE-mode has its electric field component perpendicular to the plane of incidence[1], which in the case of a wall reflection corresponds to a vertically polarized[2] wave, and vice versa for the TM-mode. The reflection coefficients for dry concrete with $\varepsilon_{\mathrm{r}} = 4.5$ are depicted in Figure 6.4. If the assumption is made that a LOS link is still feasible for large

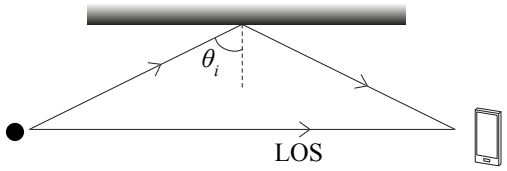

Figure 6.3: Top-down view of LOS propagation and single reflection scenario.

incident angles ($\theta_i \geq 60°$), the angles of consideration lie between $0° \leq \theta_i \leq 60°$. Thus, the reflection coefficients will be, from Figure 6.4, between $0.37 \leq |\Gamma_{\mathrm{TE}}| \leq 0.6$ and $0.07 \leq |\Gamma_{\mathrm{TM}}| \leq 0.37$ respectively. Additional losses in dB will then lie between $4.4 - 22.5\,\mathrm{dB}$, indicating the difficulty of setting up a realistic model as the additional losses may vary to a wide extent. There is no fine line separating reasonable scenarios and those non-reasonable.

The threshold level for minimum received gain will be obtained through (6.3.2) for a reasonably assumed LOS case with parametric values according to Table 6.1.

[1] The plane of incident is the plane spanned by the normal direction of the interface plane, and the propagation direction.

[2] Vertical to the earth's surface.

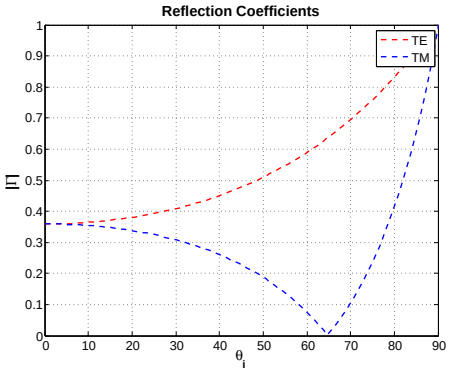

Figure 6.4: TE- and TM-mode reflection coefficents for reflection off dry concrete with $\varepsilon_{\mathrm{r}} = 4.5$.

This gives $G_{\mathrm{R,min}} = 0.6\,\mathrm{dBi}$, which can then be progressively increased to include more losses, without mentioning specific loss mechanisms.

Link Budget		
P_{T}	(dBm)	31.5
P_{R}	(dBm)	-52.3
G_{T}	(dBi)	21
d	(m)	200
L_{m}	(dB)	2.3
$\lvert\Gamma\rvert$		0
$\Rightarrow$	$G_{\mathrm{R,min}}$	0.6 dBi

Table 6.1: Values used for retrieving $G_{\mathrm{R,min}}$ in a LOS case.

It should be noted that no data from empirical studies at 15 GHz for cellular outdoor environments are so far available, which would have favoured setting up the model. Thus, the above approach should be considered as an estimate to show the viability of the beamforming concept for cellular communication.

6.4 Other Parameters for Evaluation

Apart from the coverage efficiency, there exist some other parameters that are of interest for evaluating the results:

I Maximum achievable gain.

II Total array size.

III Maximum mutual coupling, see Section 2.5. Preferably $\leq -15\,\mathrm{dB}$.

IV Elemental radiation efficiency η_{r}.

Chapter 7

Phased Array Results

In this chapter simulation results for different array configurations and diversity combinations of these are presented. The results are based on the parameters mentioned in the previous chapter.

7.1 Set-Up

The arrays are implemented in a model of a phone case to realize a more realistic environment and size restrictions. The phone case is modeled with a material of $\varepsilon_r = 3$ and $\tan\delta = 0.01$. The length, width and height of the phone case are 154 mm, 72.6 mm and 7 mm respectively, and the thickness of the material is 1.03 mm. The $\hat{\boldsymbol{z}}$-direction is set to the normal of the plane the phone spans. Referring to Section 2.10, the spacings between the elements are set to $d = \lambda_0/2$, and the phased arrays have been given different phase shift inputs, sweeping from the minimum and maximum value of the periodic parameter ($-180°$ to $180°$) with $30°$ difference:

$$\Psi_0 = -180°, -150°, \ldots, 0, \ldots, 150°, 180°$$

As $\Psi_0 = kd\cos\theta_0 = \pi\cos\theta_0$, zero phase shift gives a main lobe in the normal direction of the array orientation, and as the phase shift is increased the beam will be sweeped downwards towards the axis of the array.

The phase shift Ψ_0 is fixed, i.e. the radiated beam will have a specific direction for each phase value. This can be seen in the upcoming illustrations in Figure 7.2 and 7.9. For a 4×1 array and phase shift of $\Psi_0 = 60°$, the phase of the feed for each port will be $0°$, $60°$, $120°$ and $180°$ respectively for the four elements. The total scan pattern is obtained from the radiation patterns for all phase shifts as described in Section 6.1, p. 51.

Two contour levels will be included for illustration of the coverage efficiency. The threshold level of $G_R = 0.6$ dBi corresponds to the LOS case described in the previous chapter, while $G_R + 4.4 = 5$ dBi could be seen as a model of a minimum-loss one-reflection scenario (Section 6.3, p. 52).

7.2 SIW Arrays

The two configurations investigated are a 4×1- and a 8×1 array of SIWs respectively. The modules are implemented in the phone case as depicted in Figure 7.1 which gives for no phase shift, a main lobe in the $\hat{\boldsymbol{y}}$-direction. For fabrication simplicity, the spacing d will be set to $\lambda_0/2.3$ instead of $\lambda_0/2$, since this implies that two elements next to each other will share the same metal vias as side walls. The array size for the 4×1 array is $34.4 \times 9.9\,\mathrm{mm}^2$ and the size of the module is $41.8 \times 14.3\,\mathrm{mm}^2$. The 8×1 array is $69.2 \times 9.9\,\mathrm{mm}^2$ and the size of the module is $72.1 \times 14.3\,\mathrm{mm}^2$.

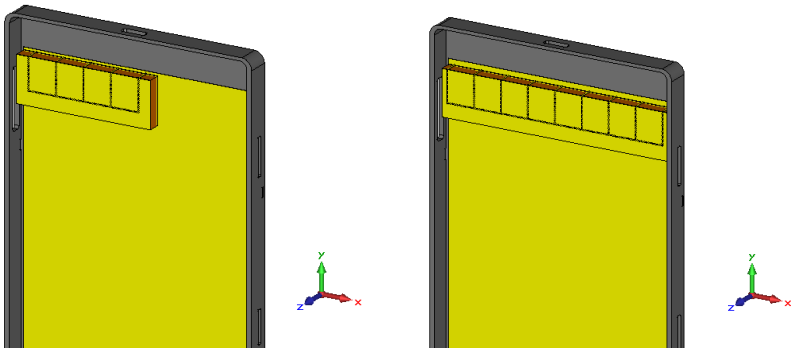

4×1 8×1

Figure 7.1: Arrays of open-ended SIWs implemented in phone case model.

For a clear insight of the beamsteering concept a 3D view of the radiation patterns for phase shifts of $\Psi = -60°,\ 0°,\ 60°$ are visible in Figure 7.2.

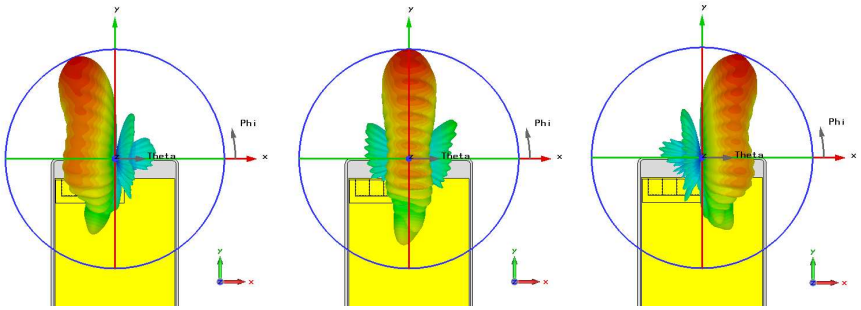

$\Psi_0 = -60°$ $\Psi_0 = 0°$ $\Psi_0 = 60°$

Figure 7.2: 3D radiation pattern for the SIW array for phase shifts $\Psi_0 = -60°, 0, 60°$.

The gain radiation pattern for phase shifts $\Psi_0 = 0°, 30°, \ldots, 180°$ can be seen in Figure 7.3 for the 4×1 array in a 2D view. Here it is visible that as the phase

shift is increased, the main beam gets steered from $\phi = 90°$ towards $\phi = 0°$. The trend is similar for the negative phase shifts, but the main beam is then steered towards $\phi = 180°$.

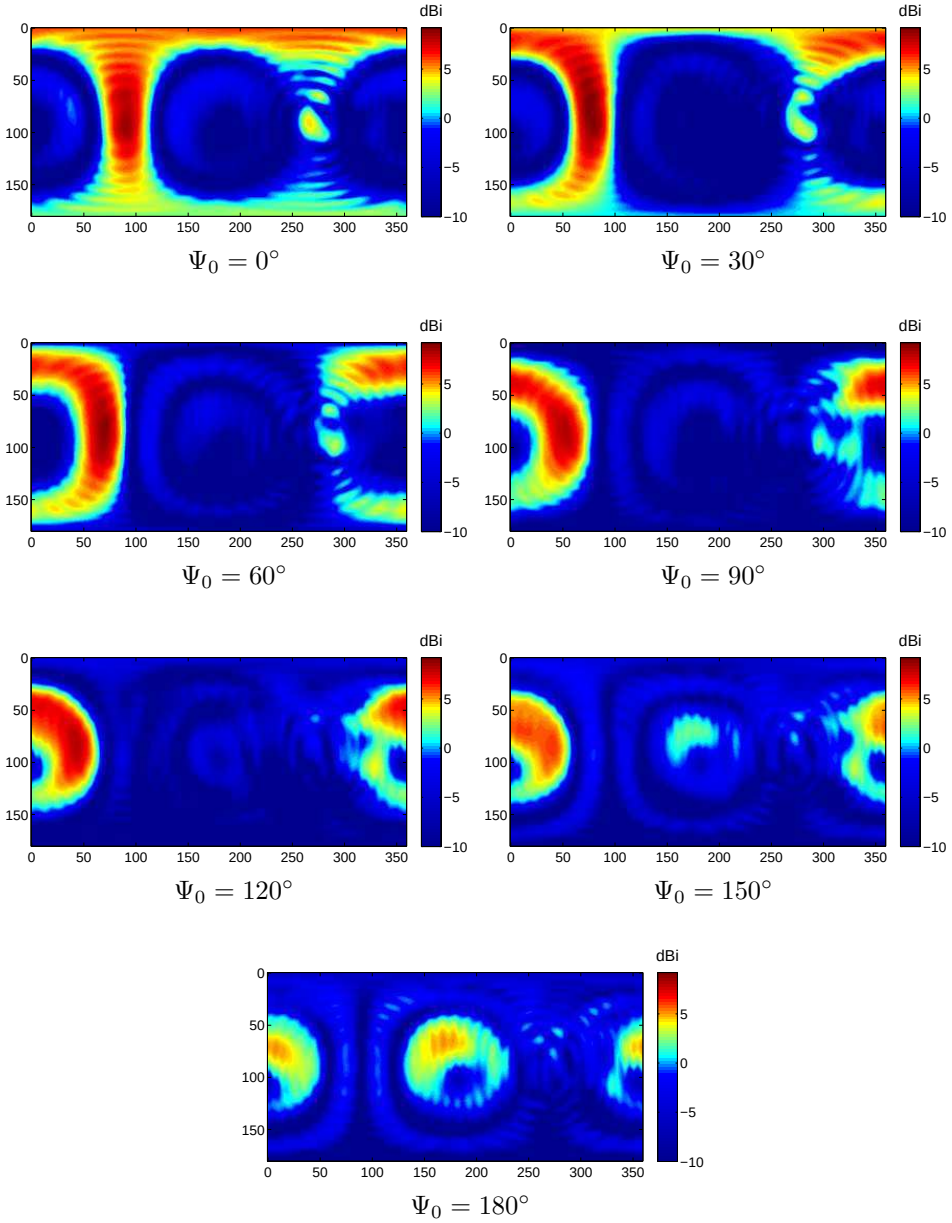

Figure 7.3: 2D radiation pattern of gain for a 4×1 SIW array, using different phase shifts Ψ_0. The x-axis denotes ϕ from $0°$ to $360°$, and the y-axis denotes θ from $0°$ to $180°$.

7.2.1 Results

All elements have a radiation efficiency between $\eta_r = 84-85\,\%$, and the maximum mutual coupling is $-11.2\,\mathrm{dB}$. The mutual coupling can be seen together with the reflection coefficient in Figure 7.4. The total scan pattern obtained from all phase shifts $\Psi_0 = -180°, \ldots, 180°$ can be seen in Figure 7.5 for the 4×1 array, and in Figure 7.6 for the 8×1 array. The contours in the figures denote the two threshold levels of $G_\mathrm{R} = 0.6\,\mathrm{dBi}$ (blue to green) and $G_\mathrm{R} = 5\,\mathrm{dBi}$ (yellow to red).

For the 4×1 array, the coverage efficiency with respect to the two levels are $\eta_c = 82.6\,\%$ and $\eta_c = 43\,\%$ respectively. The maximum gain achieved is $G_\mathrm{max} = 9.2\,\mathrm{dBi}$.

For the 8×1 array, the coverage efficiency with respect to the two levels are $\eta_c = 93.6\,\%$ and $\eta_c = 56.9\,\%$ respectively. The maximum gain achieved is $G_\mathrm{max} = 11.9\,\mathrm{dBi}$.

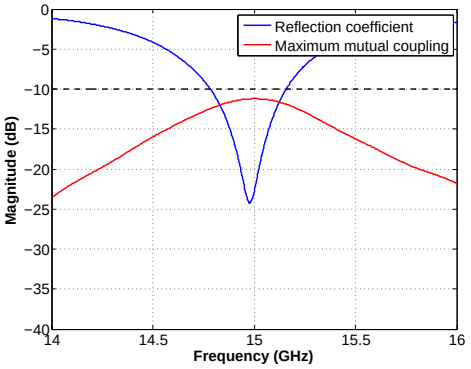

Figure 7.4: Reflection coefficient (blue) and maximum mutual coupling (red) in dB-scale.

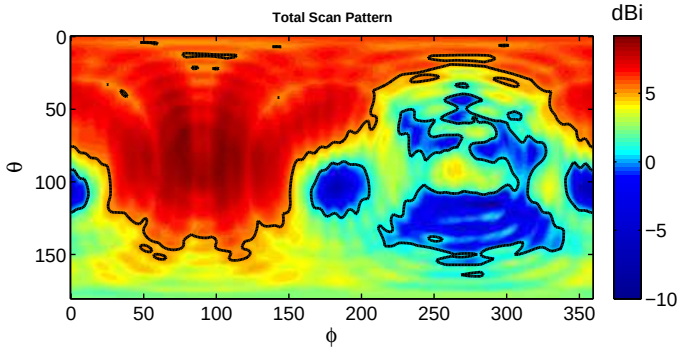

Figure 7.5: Total scan pattern from all phase shifts of the 4×1 SIW array. The contours marks the threshold levels of $G_\mathrm{R} = 0.6\,\mathrm{dBi}$ and $G_\mathrm{R} = 5\,\mathrm{dBi}$ respectively.

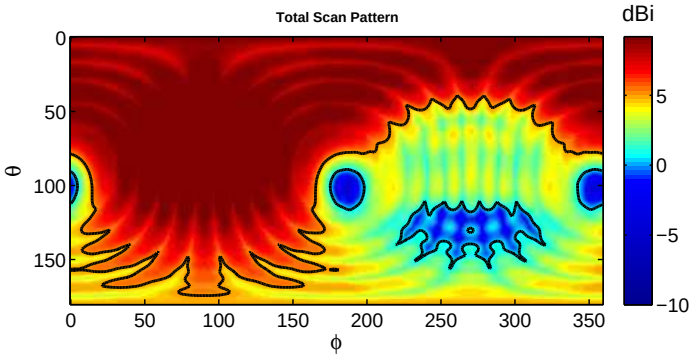

Figure 7.6: Total scan pattern from all phase shifts of the 8×1 SIW array. The contours marks the threshold levels of $G_{\mathrm{R}} = 0.6\,\mathrm{dBi}$ and $G_{\mathrm{R}} = 5\,\mathrm{dBi}$ respectively.

The coverage efficiency as a function of minimum received gain G_{R} can be seen in Figure 7.7 for both array configurations. As the use of more elements raises the achieved gain, it is noticable that for the same value of η_{c}, the minimum G_{R} is mainly shifted $\sim 2.5\,\mathrm{dBi}$ to the right by using a 8×1 array. Moreover, it is noticeable in both Figure 7.5 and 7.6 that the region with worst coverage is the region surrounding $\theta = 90°$, $\phi = 270°$, corresponding to the region opposite to the direction the arrays are radiating. All simulated results of the SIW arrays are listed in Table 7.1.

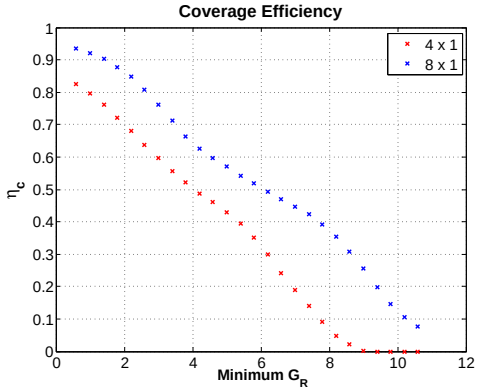

Figure 7.7: Coverage efficiency η_{c} as a function of minimum received gain G_{R}. Red crosses - 4×1. Blue crosses - 8×1.

4×1 SIW Array	
Array (mm^2)	34.4×9.9
Module (mm^2)	41.8×14.3
Element η_r	$84 - 85\,\%$
Coupling (dB)	-11.2
G_{max} (dBi)	9.2
η_c	
$G_R = 0.6\,dBi$	82.6 %
$G_R = 5\,dBi$	43.0 %

8×1 SIW Array	
Array (mm^2)	69.2×9.9
Module (mm^2)	72.1×14.3
Element η_r	$84 - 85\,\%$
Coupling (dB)	-11.2
G_{max} (dBi)	11.9
η_c	
$G_R = 0.6\,dBi$	93.6 %
$G_R = 5\,dBi$	56.9 %

Table 7.1: Listed results of the 4×1- and 8×1 SIW arrays. Coupling denotes the maximum mutual coupling.

7.3 DRA Arrays

The two configurations investigated are a 4×1- and a 8×1 array of DRAs respectively. The modules are implemented in the phone case as depicted in Figure 7.8 which gives for no phase shift, a main lobe in the $\hat{z}$-direction. The array size for the 4×1 array is $34.3 \times 15\,\mathrm{mm}^2$ and the size of the module is $45 \times 15\,\mathrm{mm}^2$. The 8×1 array is $74.3 \times 15\,\mathrm{mm}^2$ and the size of the module is $85 \times 15\,\mathrm{mm}^2$.

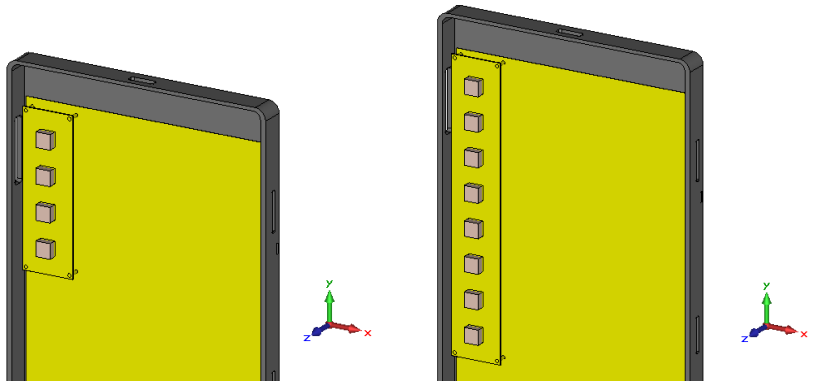

4×1 8×1

Figure 7.8: Arrays of DRAs implemented in phone case model.

For a clear insight of the beamsteering concept a 3D view of the radiation patterns for phase shifts of $\Psi = -60°,\ 0°,\ 60°$ are visible in Figure 7.9.

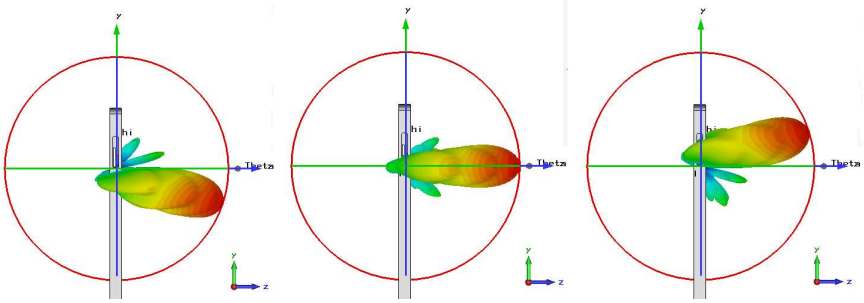

$\Psi_0 = -60°$ $\Psi_0 = 0°$ $\Psi_0 = 60°$

Figure 7.9: 3D radiation pattern for the DRA array for phase shifts $\Psi_0 = -60°, 0, 60°$.

The gain radiation pattern for phase shifts $\Psi_0 = 0°, 30°, \ldots, 180°$ can be seen in Figure 7.10 for the 4×1 array in a 2D view. Here it is visible that as the phase shift is increased, the main beam gets steered from $\theta = 0°$ towards $\theta = 90°$ at $\phi = 90°$. The trend is similar for the negative phase shifts, but the main beam is then steered towards $\theta = 90°$ at $\phi = 270°$.

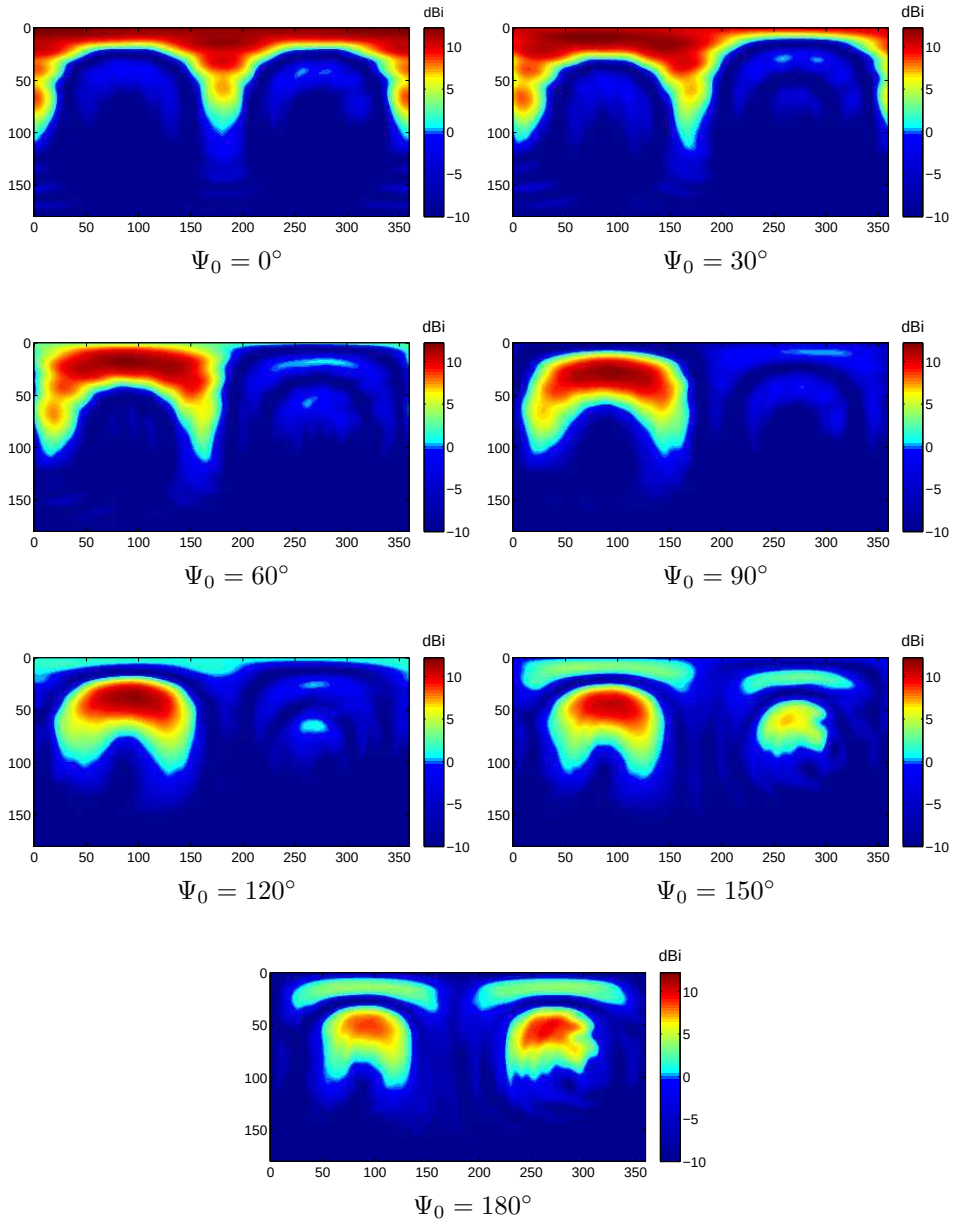

Figure 7.10: 2D radiation pattern of gain for a 4×1 SIW array, using different phase shifts Ψ_0. The x-axis denotes ϕ from $0°$ to $360°$, and the y-axis denotes θ from $0°$ to $180°$.

7.3.1 Results

All elements have a radiation efficiency between $\eta_r = 95 - 96\,\%$, and the maximum mutual coupling is $-16.8\,\mathrm{dB}$. The mutual coupling can be seen together with the

reflection coefficient in Figure 7.11. The total scan pattern obtained from all phase shifts $\Psi_0 = -180°, \ldots, 180°$ can be seen in Figure 7.12 for the 4×1 array, and in Figure 7.13 for the 8×1 array. The contours in the figures denote the two threshold levels of $G_{\mathrm{R}} = 0.6\,\mathrm{dBi}$ (blue to green) and $G_{\mathrm{R}} = 5\,\mathrm{dBi}$ (yellow to red).

For the 4×1 array, the coverage efficiency with respect to the two levels are $\eta_{\mathrm{c}} = 58.2\,\%$ and $\eta_{\mathrm{c}} = 38.9\,\%$ respectively. The maximum gain achieved is $G_{\max} = 12.2\,\mathrm{dBi}$.

For the 8×1 array, the coverage efficiency with respect to the two levels are $\eta_{\mathrm{c}} = 65.4\,\%$ and $\eta_{\mathrm{c}} = 50.2\,\%$ respectively. The maximum gain achieved is $G_{\max} = 15.1\,\mathrm{dBi}$.

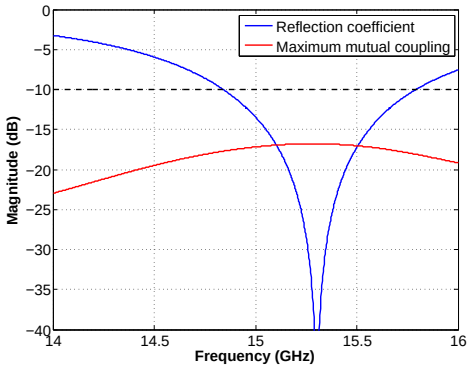

Figure 7.11: Reflection coefficient (blue) and maximum mutual coupling (red) in dB-scale.

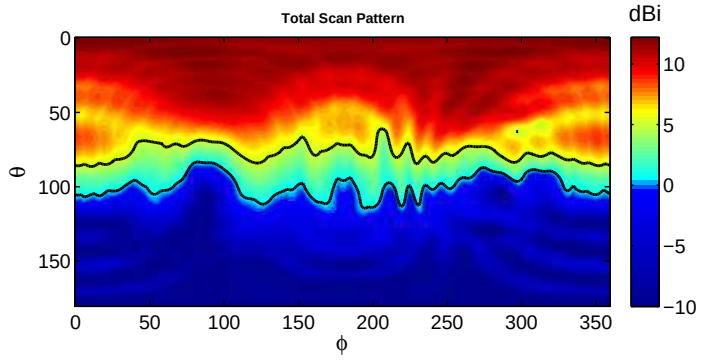

Figure 7.12: Total scan pattern from all phase shifts of the 4×1 DRA array. The contours marks the threshold levels of $G_{\mathrm{R}} = 0.6\,\mathrm{dBi}$ and $G_{\mathrm{R}} = 5\,\mathrm{dBi}$ respectively.

The coverage efficiency as a function of minimum received gain G_{R} can be seen in Figure 7.14 for both array configurations. As the use of more elements raises the achieved gain, it is noticable that for the same value of η_{c}, the minimum G_{R} is

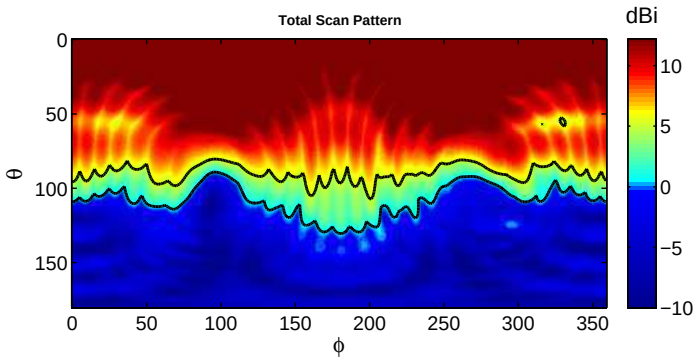

Figure 7.13: Total scan pattern from all phase shifts of the 8×1 DRA array. The contours marks the threshold levels of $G_{\mathrm{R}} = 0.6\,\mathrm{dBi}$ and $G_{\mathrm{R}} = 5\,\mathrm{dBi}$ respectively.

mainly shifted $\sim 2.5\,\mathrm{dBi}$ to the right by using a 8×1 array. Moreover, the increase of the number of elements can not contribute to much more coverage in the lower hemisphere, as the DRA has a broadside radiation. All simulated results of the DRA arrays are listed in Table 7.2.

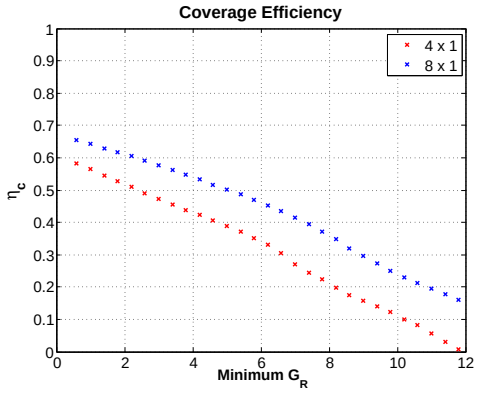

Figure 7.14: Coverage efficiency η_{c} as a function of minimum received gain G_{R}. Red crosses - 4×1. Blue crosses - 8×1.

4×1 DRA Array	
Array (mm^2)	34.3×15
Module (mm^2)	45×15
Element η_r	$95 - 96\,\%$
Coupling (dB)	-16.8
G_max (dBi)	12.2
η_c	
$G_\mathrm{R} = 0.6\,\mathrm{dBi}$	$58.2\,\%$
$G_\mathrm{R} = 5\,\mathrm{dBi}$	$38.9\,\%$

8×1 DRA Array	
Array (mm^2)	74.3×15
Module (mm^2)	85×15
Element η_r	$95 - 96\,\%$
Coupling (dB)	-16.8
G_max (dBi)	15.1
η_c	
$G_\mathrm{R} = 0.6\,\mathrm{dBi}$	$65.4\,\%$
$G_\mathrm{R} = 5\,\mathrm{dBi}$	$50.2\,\%$

Table 7.2: Listed results of the 4×1- and 8×1 DRA arrays. Coupling denotes the maximum mutual coupling.

7.4 Patch Arrays

The two configurations investigated are a 4×1- and a 8×1 array of patches respectively. The modules are implemented in the phone case as depicted in Figure 7.15 which gives for no phase shift, a main lobe in the $\hat{\boldsymbol{z}}$-direction. The array size for the 4×1 array is $37 \times 15\,\mathrm{mm}^2$ and the size of the module is $45 \times 15\,\mathrm{mm}^2$. The 8×1 array is $77 \times 15\,\mathrm{mm}^2$ and the size of the module is $85 \times 15\,\mathrm{mm}^2$.

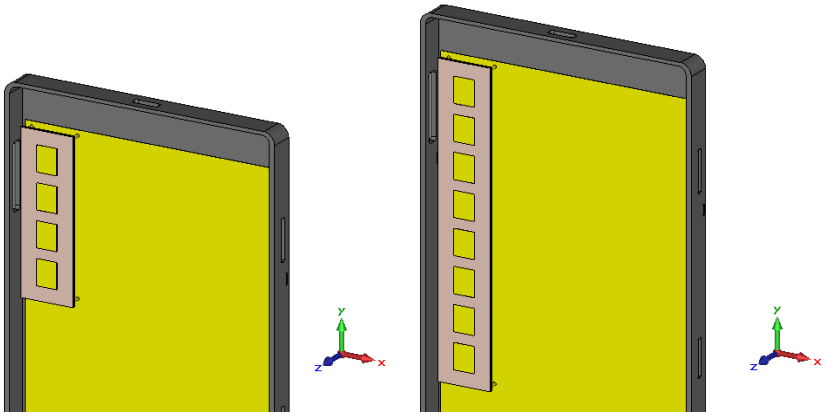

Figure 7.15: Arrays of patches implemented in phone case model.

Due to the similarities in radiation pattern between the DRA and the patch, both figures showing the 3D view and the gain radiation pattern for each individual phase shift will be excluded.

7.4.1 Results

All elements have a radiation efficiency between $\eta_\mathrm{r} = 92 - 93\,\%$, and the maximum mutual coupling is $-15.2\,\mathrm{dB}$. The mutual coupling can be seen together with the reflection coefficient in Figure 7.16. The total scan pattern obtained from all phase shifts $\Psi_0 = -180°, \ldots, 180°$ can be seen in Figure 7.17 for the 4×1 array, and in Figure 7.18 for the 8×1 array. The contours in the figures denote the two threshold levels of $G_\mathrm{R} = 0.6\,\mathrm{dBi}$ (blue to green) and $G_\mathrm{R} = 5\,\mathrm{dBi}$ (yellow to red).

For the 4×1 array, the coverage efficiency with respect to the two levels are $\eta_\mathrm{c} = 50.4\,\%$ and $\eta_\mathrm{c} = 34.7\,\%$ respectively. The maximum gain achieved is $G_\mathrm{max} = 12.4\,\mathrm{dBi}$.

For the 8×1 array, the coverage efficiency with respect to the two levels are $\eta_\mathrm{c} = 60.4\,\%$ and $\eta_\mathrm{c} = 45.0\,\%$ respectively. The maximum gain achieved is $G_\mathrm{max} = 15.1\,\mathrm{dBi}$.

The coverage efficiency as a function of minimum received gain G_R can be seen in Figure 7.19 for both array configurations. As the use of more elements raises the achieved gain, it is noticable that for the same value of η_c, the minimum G_R is mainly shifted $\sim 3\,\mathrm{dBi}$ to the right by using a 8×1 array. Moreover, the increase

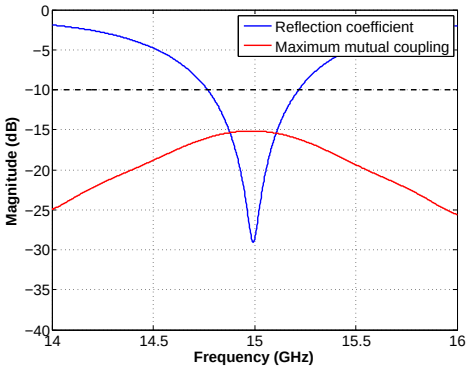

Figure 7.16: Reflection coefficient (blue) and maximum mutual coupling (red) in dB-scale.

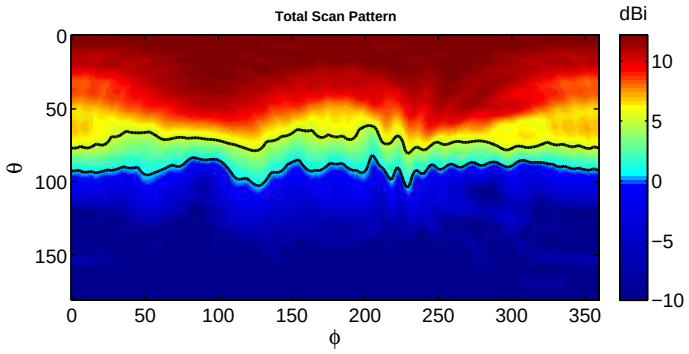

Figure 7.17: Total scan pattern from all phase shifts of the 4×1 patch array. The contours marks the threshold levels of $G_{\mathrm{R}} = 0.6\,\mathrm{dBi}$ and $G_{\mathrm{R}} = 5\,\mathrm{dBi}$ respectively.

of the number of elements can not contribute to much more coverage in the lower hemisphere, as the patch has a broadside radiation. All simulated results of the patch arrays are listed in Table 7.3.

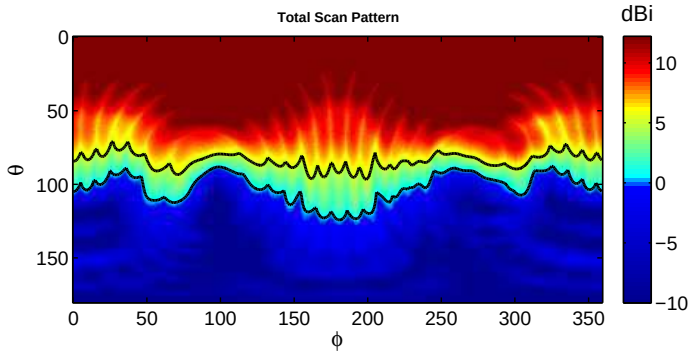

Figure 7.18: Total scan pattern from all phase shifts of the 8×1 patch array. The contours marks the threshold levels of $G_{\mathrm{R}} = 0.6\,\mathrm{dBi}$ and $G_{\mathrm{R}} = 5\,\mathrm{dBi}$ respectively.

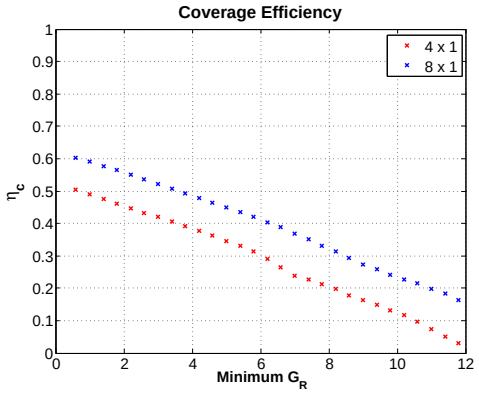

Figure 7.19: Coverage efficiency η_{c} as a function of minimum received gain G_{R}. Red crosses - 4×1. Blue crosses - 8×1.

4×1 Patch Array	
Array (mm^2)	37×15
Module (mm^2)	45×15
Element η_{r}	$92 - 93\,\%$
Coupling (dB)	-15.2
$G_{\max}$ (dBi)	12.4
η_{c}	
$G_{\mathrm{R}} = 0.6\,\mathrm{dBi}$	$50.4\,\%$
$G_{\mathrm{R}} = 5\,\mathrm{dBi}$	$34.7\,\%$

8×1 Patch Array	
Array (mm^2)	77×15
Module (mm^2)	85×15
Element η_{r}	$92 - 93\,\%$
Coupling (dB)	-15.2
$G_{\max}$ (dBi)	15.1
η_{c}	
$G_{\mathrm{R}} = 0.6\,\mathrm{dBi}$	$60.4\,\%$
$G_{\mathrm{R}} = 5\,\mathrm{dBi}$	$45.0\,\%$

Table 7.3: Listed results of the 4×1- and 8×1 patch arrays. Coupling denotes the maximum mutual coupling.

7.5 Motivation of Choice for Subarray Systems

The performances of the single array systems presented in the previous chapters can be used to support the choice of promising subarray configurations. The coverage efficiency as a function of minimum received gain G_{R} can be seen in Figure 7.20 for the 4×1 arrays of all three designs. The edge radiating SIW array can be seen to show good promise, and is only inferior to the DRA and the patch when it comes to maximum achieved gain. As a consequence, its coverage efficiency is then lower for high values of G_{R}.

Increasing the number of elements improves the efficiency. The overall gain is increased but the radiation pattern stays similar, thus low-coverage areas will not be complemented by adding elements in the arrays. It can also be stated that 8×1 array configurations have sizes in the vicinity of the available width in the phone case. Using a subarray system, it can then be reasonable to stick to two 4×1 arrays in order to not overuse space.

The purpose of combining is to achieve complementary coverage. The chosen configurations are thus a system of two 4×1 arrays using at least one edge radiating SIW array. Two configurations using two SIW arrays will be further investigated; a top-bottom and a top-side one. Moreover, two configurations using a SIW array combined with a DRA array will be further investigated to see if this could increase the overall coverage. Due to the similar achieved performances of the DRA- and the patch arrays, configurations using patch arrays will be excluded from the upcoming sections.

The two arrays in all the following subarray configurations are fed independently, with separate phase shift inputs for the respective arrays.

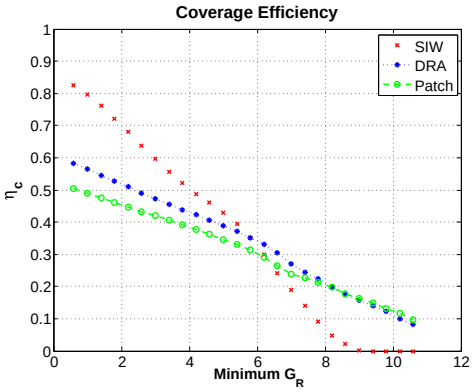

Figure 7.20: Coverage efficiency η_{c} as a function of minimum received gain G_{R} for 4×1 arrays of all three designs.

7.6 Subarrays Using SIWs and DRAs

The chosen configurations are a 4×1 SIW array together with a 4×1 DRA array using two different alignments, as depicted in Figure 7.21. The array sizes remain from the previous sections. Thus for the parallel alignment, the phone case width has been slightly increased in order to make room for both modules. The width is in this case set to 87.1 mm instead of 72.6 mm. The parallel alignment allows for the beam from the DRA array to be sweeped between $\phi = 0°$ and $\phi = 180°$ in an arch in the xz-plane. For the perpendicular alignment, the beam from the DRA array is sweeped between $\phi = 90°$ and $\phi = 270°$ in an arch in the yz-plane.

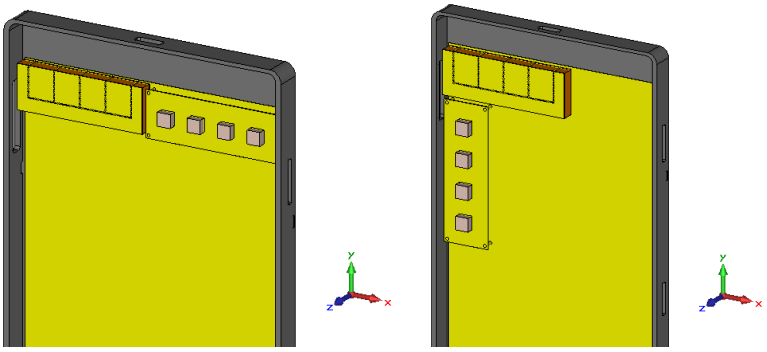

Config. 1: Parallel alignment.

Config. 2: Perpendicular alignment.

Figure 7.21: Two configurations of subarray systems using one SIW array and one DRA array implemented in phone case model.

7.6.1 Results

The total scan pattern obtained from all phase shifts $\Psi_0 = -180°, \ldots, 180°$ can be seen in Figure 7.22 for the parallel alignment, and in Figure 7.23 for the perpendicular alignment. The contours in the figures denote the two threshold levels of $G_{\mathrm{R}} = 0.6\,\mathrm{dBi}$ (blue to green) and $G_{\mathrm{R}} = 5\,\mathrm{dBi}$ (yellow to red). The coverage efficiency as a function of minimum received gain G_{R} can be seen in Figure 7.24 for both configurations. The respective efficiencies for the two levels are listed in Table 7.4 and compared to what has been obtained for a single 4×1 SIW array.

Referring to Figure 7.24, it can be clearly stated that the orientation of the DRA array has little effect on the obtained efficiency and that the contribution from the DRA array is small in both cases. It can also be seen by looking at Figure 7.22 and 7.23, that there is still the issue of achieving coverage in the region surrounding $\theta = 90°$, $\phi = 270°$.

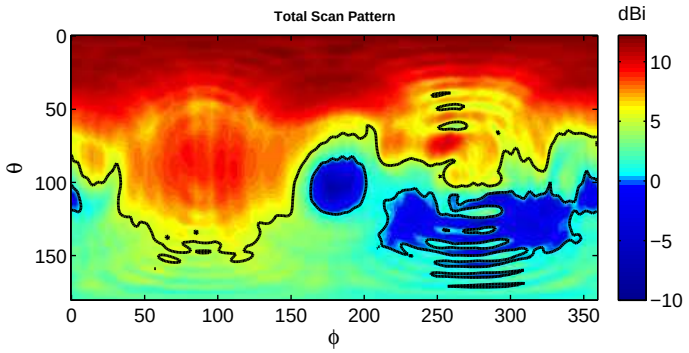

Figure 7.22: Total scan pattern from all phase shifts of the parallel alignment using one SIW- and one DRA array. The contours marks the threshold levels of $G_{\mathrm{R}} = 0.6\,\mathrm{dBi}$ and $G_{\mathrm{R}} = 5\,\mathrm{dBi}$ respectively.

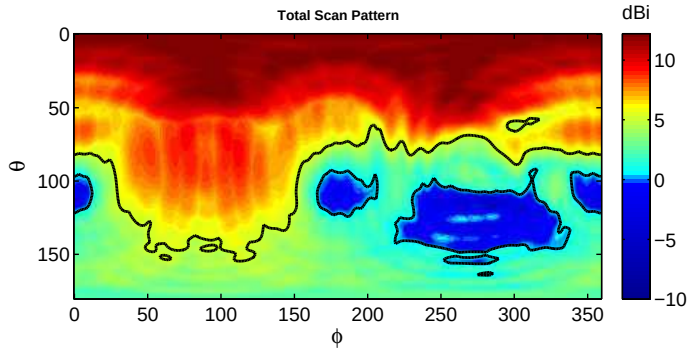

Figure 7.23: Total scan pattern from all phase shifts of the perpendicular alignment using one SIW- and one DRA array. The contours marks the threshold levels of $G_{\mathrm{R}} = 0.6\,\mathrm{dBi}$ and $G_{\mathrm{R}} = 5\,\mathrm{dBi}$ respectively.

	Parallel	Perpendicular	4×1 SIW
η_{c} (%)			
$G_{\mathrm{R}} = 0.6\,\mathrm{dBi}$	87.8	88.4	82.6
$G_{\mathrm{R}} = 5\,\mathrm{dBi}$	58.5	55.9	43.0

Table 7.4: Listed efficiencies for the subarray systems compared with a single 4×1 SIW array, at the two threshold levels.

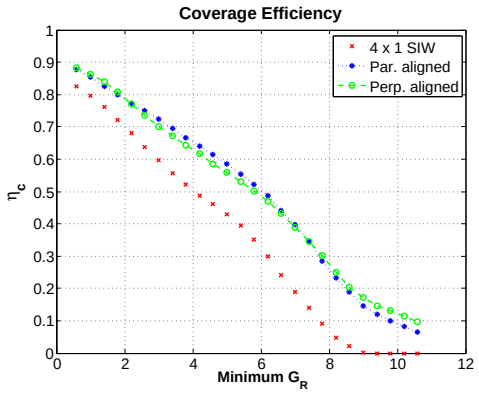

Figure 7.24: Coverage efficiency η_{c} as a function of minimum received gain G_{R}. Red denotes the single 4×1 SIW array, blue the parallel aligned configuration and green the perpendicular aligned configuration.

7.7 Subarrays Using Two SIWs

The chosen configurations are two subarray systems using two 4×1 SIW arrays, as depicted in Figure 7.25. The top-side configuration allows for two mainbeams ($\Psi_0 = 0°$) in the $\hat{\boldsymbol{x}}$- and $\hat{\boldsymbol{y}}$-direction respectively, while the top-bottom configuration allows for two mainbeams in the $\pm\hat{\boldsymbol{y}}$-directions.

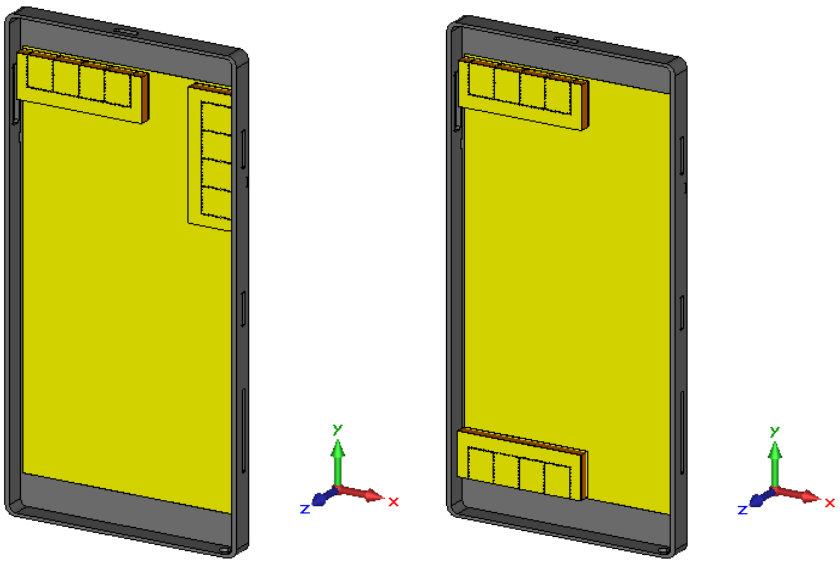

Config. 1: Top-Side Config. 2: Top-Bottom

Figure 7.25: Two configurations of subarray systems using two SIW arrays implemented in phone case model.

7.7.1 Results

The total scan pattern obtained from all phase shifts $\Psi_0 = -180°, \ldots, 180°$ can be seen in Figure 7.26 for the top-side configuration, and in Figure 7.27 for the top-bottom configuration. The contours in the figures denote the two threshold levels of $G_{\mathrm{R}} = 0.6\,\mathrm{dBi}$ (blue to green) and $G_{\mathrm{R}} = 5\,\mathrm{dBi}$ (yellow to red). The coverage efficiency as a function of minimum received gain G_{R} can be seen in Figure 7.28 for both configurations. The respective efficiencies for the two levels are listed in Table 7.5 and compared to what has been obtained for a single 4×1 SIW array.

In Figure 7.28 it is visible how the coverage is significantly increased by using more than one SIW array. For both configurations, η_{c} is increased with around 15 percentage points for $G_{\mathrm{R}} = 0.6\,\mathrm{dBi}$ and more than 20 percentage points for $G_{\mathrm{R}} = 5\,\mathrm{dBi}$. Comparing the total scan pattern for a single SIW array (Figure 7.5) with Figure 7.26 and 7.27, it can be seen that the low-coverage area around $\theta = 90°$, $\phi = 270°$ can be successfully covered by the top-bottom configuration and to some extent by the top-side configuration.

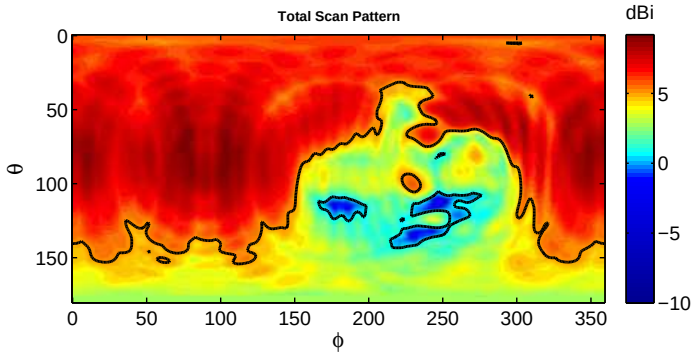

Figure 7.26: Total scan pattern from all phase shifts of the top-side configuration of two SIW arrays. The contours marks the threshold levels of $G_{\mathrm{R}} = 0.6\,\mathrm{dBi}$ and $G_{\mathrm{R}} = 5\,\mathrm{dBi}$ respectively.

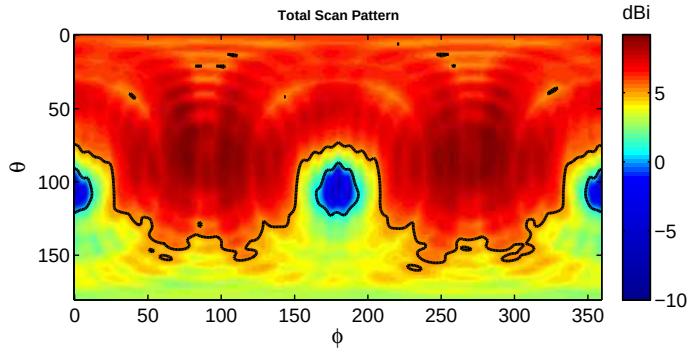

Figure 7.27: Total scan pattern from all phase shifts of the top-bottom configuration of two SIW arrays. The contours marks the threshold levels of $G_{\mathrm{R}} = 0.6\,\mathrm{dBi}$ and $G_{\mathrm{R}} = 5\,\mathrm{dBi}$ respectively.

	Top-Side	Top-Bottom	4×1 SIW
η_{c} (%)			
$G_{\mathrm{R}} = 0.6\,\mathrm{dBi}$	97.7	97.3	82.6
$G_{\mathrm{R}} = 5\,\mathrm{dBi}$	64.3	73.1	43.0

Table 7.5: Listed efficiencies for the subarray systems compared with a single 4×1 SIW array, at the two threshold levels.

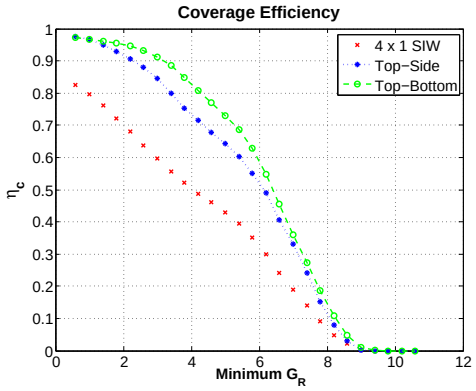

Figure 7.28: Coverage efficiency η_{c} as a function of minimum received gain G_{R}. Red denotes the single 4×1 SIW array, blue the top-side configuration and green the top-bottom configuration.

Chapter 8

Summary and Conclusions

In this thesis, a literature study of recent advancements in mmWave technology has been carried out, to point out the state of the art within the topic. Printed antennas are commonly proposed designs, mostly because of their low fabrication costs and small footprints. Moreover, printed antennas can be combined with many different enhancement techniques, which can be applied through multilayer technology. DRAs can be seen as an alternative to the printed patch antenna, with similar characteristics but exhibits less losses at higher frequencies. The relatively novel SIW technology enables for the antenna element to be integrated with other circuits on a single substrate.

Primary designs of an aperture coupled patch, an aperture coupled DRA and a probe fed open-ended SIW have been designed and simulated using CST at operational frequencies 15 GHz and 28 GHz. The DRA exhibits the widest bandwidth (6 %) and highest radiation efficiency (96 %), while the SIW has the narrowest bandwidth (2 %) and lowest radiation efficiency (85 %). The narrow bandwidth can be seen to depend on the choice of probe as a feed more than the antenna element itself, and could possibly be enhanced by another transition technique.

Array configurations of the three designs have been implemented in a phone case model, and given different phase shift inputs to enable beamsteering. The arrays have been evaluated based on their total scan pattern obtained from the radiation pattern of each phase shift. The different radiation patterns and number of elements have been examined to see what characteristics show good promise for a mobile terminal antenna array. This part aims to illustrate the characterization of phased array systems through the achievable coverage (the coverage efficiency) of the total scan pattern using many phase shifts. Maximum mutual coupling is largest for the SIW array and lowest for the DRA array. For a 4×1 array configuration, maximum gain is around 12 dBi for the patch- and DRA array, and 9 dBi for the SIW array.

The SIW array radiate at its edges, which shows good promise in achieving a high coverage efficiency if a subarray system is applied. The DRA and patch antenna array accomplish a broadside radiation that can achieve coverage over one hemisphere. An 8 element array at 15 GHz has a length in the order of the total width of the phone case, thus it can be seen to be the spatial limit of array systems for this frequency. A system using two 4×1 subarrays shows more promise than using one 8×1 array, which can be interpreted as a subarray system manages to cover a larger solid angle instead of increasing the overall gain.

Chapter 9
Future Work

As mmWave frequencies for cellular communication is a relatively new research front, the future work covers a large range of work in different areas. Moreover, the 15 GHz band has not gained as much attention as other higher bands (28, 38 GHz and 60 GHz), wherefore one key aspect is to carry out empirical studies to characterize the channel model more thoroughly.

The impact of the material cover enclosing the antennas has not been included in the study. Including the whole cover will detune the operational frequency, wherefore chosen antenna designs should be redesigned and studied with added material cover. Further, the user's body effect on the antenna need to be included to study the impact on the radiation pattern and matching.

The SIW showed good performance in terms of coverage, however its bandwidth was relatively narrow. Bandwidth enhancement techniques, or other antenna designs based on SIW technology can be looked more closely into. Proposed ideas are to use a different kind of feeding technique, such as a tapered microstrip. The linearly tapered slot in [29] is an edge radiating element with a large bandwidth constructed using SIW technology. Other antenna types that also exhibits edge radiation could preferably also be investigated to see if there exist better alternatives with similar radiation characteristics.

If a subarray system of broadside radiating arrays, e.g. using patches or DRAs, could be implemented to radiate in direct opposite directions, they could target one hemisphere each which would enhance the obtained coverage. Future investigations could be done in using this kind of arrangement.

The underlying feed network should also be included in the models in order to realize models ready for fabrication.

Finally when good models are obtained, mock-ups should be fabricated in order to compare simulated and measured results.

References

[1] T. S. Rappaport. Millimeter Wave Mobile Communications for 5G Cellular: It Will Work! *IEEE Access*, 1:335–349, 2013.

[2] Y. P. Zhang. Integration of Array Antennas in Chip Package for 60-GHz Radios. *Proceedings of the IEEE*, 100(7):2364–2371, July 2012.

[3] J. Wells. Faster Than Fiber: The Future of Multi-Gb/s Wireless. *IEEE Microwave Magazine*, (May):104–112, 2009.

[4] IEEE145-1993. IEEE Standard Definition of Terms for Antennas, March 1993.

[5] Sophocles J. Orfanidis. Electromagnetic waves and antennas, 2002. `www.ece.rutgers.edu/~orfanidi/ewa`, revision date June 21, 2004.

[6] P. Bhartia and R. Garg. *Microstrip Antenna Design Handbook*. Artech House, 2001.

[7] Y.P. Zhang and D. Liu. Antenna-on-Chip and Antenna-in-Package Solutions to Highly Integrated Millimeter-Wave Devices for Wireless Communications. *IEEE Transactions on Antennas and Propagation*, 57(10):2830–2841, 2009.

[8] T. S. Rappaport, J. N. Murdock, and F. Gutierrez. State of the Art 60 GHz ICs and Systems for Wireless Communications. *Proceedings of the IEEE*, 99(8):1390–1436, 2011.

[9] F. Gutierrez and S. Agarwal. On-chip Integrated Antenna Structures in CMOS for 60 GHz WPAN Systems. *IEEE Journal on Selected Areas in Communications*, 27(8):1367–1378, 2009.

[10] E. Öjefors. *Micromachined Antennas for Integration with Silicon Based Active Devices*. PhD thesis, Faculty of Science and Technology, Uppsala University, 2006.

[11] S-S. Hsu and K-C. Wei. A 60-GHz Millimeter-Wave CPW-Fed Yagi Antenna Fabricated by Using $0.18 - \mu$m CMOS Technology. *IEEE Electron Device Letters*, 29(6):625–627, 2008.

[12] S. M. Sze and G. S. May. *Fundamentals of Semiconductor Fabrication*. John Wiley & Sons, 2004.

[13] D.G. Kam, D. Liu, et al. Low-cost Antenna-in-Package Solutions for 60-GHz Phased-Array Systems. *2010 IEEE, Conference on EPEPS*, 19:93–96, 2010.

[14] T. Zwick, D. Liu, et al. Broadband Planar Superstrate Antenna for Integrated Millimeterwave Transceivers. *IEEE Transactions on Antennas and Propagation*, 54(10):2790–2796, 2006.

[15] M. Sun, Y. P. Zhang, et al. Integration of Yagi Antenna in LTCC Package for Differential 60-GHz Radio. *IEEE Transactions on Antennas and Propagation*, 56(8):2780–2783, 2008.

[16] W. Hong, A. Goudelev, et al. Monolithic Circular Stacked Antenna Array using High-volume LTCC technology for 60 GHz. *AP-S/URSI*, pages 2032–2034, 2011.

[17] D. Liu, H.C. Chen, et al. An LTCC Superstrate Patch Antenna for 60-GHz Package Applications. *AP-S/URSI*, (1):2–5, 2010.

[18] A. E. I. Lamminen, J. Säily, et al. 60-GHz Patch Antennas and Arrays on LTCC With Embedded-Cavity Substrates. *IEEE Transactions on Antennas and Propagation*, 56(9):2865–2874, 2008.

[19] A-C. Bunea, D. Neculoiu, et al. LTCC Microstrip Parasitic Patch Antenna for 77 GHz Automotive Applications. *IEEE International COMCAS*, 1(October):21–23, 2013.

[20] D. Liu, J. Akkermans, and B. Floyd. A Superstrate Patch Antenna for 60-GHz Applications. *IEEE Transactions on Antennas and Propagation*, pages 2592–2594, 2009.

[21] J.G. Kim, H.S. Lee, et al. 60-GHz CPW-fed Post-Supported Patch Antenna using Micromachining Technology. *IEEE Microwave and Wireless Components Letters*, 15(10):635–637, 2005.

[22] A. A. Hanzaz. LTCC System for High Frequency Applications. *Proceedings of the IMECS*, 2:14–17, 2012.

[23] http://www.rogerscorp.com, 2014.

[24] P.V. Bijumon, A.P. Freundorfer, et al. High Gain On-Chip Dielectric Resonator Antennas Using Silicon Technology for Millimeter Wave Wireless Links. *2007 IEEE, Canadian Conference on ECE*, (10):804–807, 2007.

[25] H. Chorfi, M. Nedil, et al. Design of a 60 GHz Dielectric Resonator Antenna Array mounted on a Conformal Structure. *IEEE Transactions on Antennas and Propagation*, (1):4–5, 2012.

[26] W. M. A. Wahab, Busuioc D., et al. Low Cost Planar Waveguide Technology-Based Dielectric Resonator Antenna (DRA) for Millimeter-Wave Applications: Analysis, Design, and Fabrication. *IEEE Transactions on Antennas and Propagation*, 58(8):2499–2507, 2010.

[27] Q. Lai, C. Fumeaux, et al. 60 GHz Aperture-Coupled Dielectric Resonator Antennas Fed by a Half-Mode Substrate Integrated Waveguide. *IEEE Transactions on Antennas and Propagation*, 58(6):1856–1864, 2010.

[28] K. Wu, Y.J. Cheng, et al. Millimeter-Wave Integrated Waveguide Antenna Arrays and Beamforming Networks for Low-Cost Satellite and Mobile Systems. *Antenna and Propagation (EuCAP)*, pages 1–5, 2010.

[29] Y.J. Cheng, W. Hong, et al. Design of a Monopulse Antenna Using a Dual V-Type Linearly Tapered Slot Anenna (DVLTSA). *IEEE Transactions on Antennas and Propagation*, 56(9):2903–2909, 2008.

[30] Y. J. Cheng and Y. Fan. Millimeter-Wave Miniaturized Substrate Integrated Multibeam Antenna. *IEEE Transactions on Antennas and Propagation*, 59(12):4840–4844, December 2011.

[31] X.P. Chen, K. Wu, et al. Low-Cost High Gain Planar Antenna Array for 60-GHz Band Applications. *IEEE Transactions on Antennas and Propagation*, 58(6):2126–2129, 2010.

[32] J-C. S. Chieh, A-V. Pham, et al. A Low Cost 8 x 8 W-Band Substrate Integrated Waveguide Antenna Array Detector on LCP. *Microwave and Optical Technology Letters*, 55(8):1825–1830, 2012.

[33] H. Wang, D-G. Fang, et al. Dielectric Loaded Substrate Integrated Waveguide (SIW) H-Plane Horn Antennas. *IEEE Transactions on Antennas and Propagation*, 58(3):640–647, 2010.

[34] K.B. Ng, H. Wong, et al. 60 GHz Plated Through Hole Printed Magneto-Electric Dipole Antenna. *IEEE Transactions on Antennas and Propagation*, 60(7):3129–3136, July 2012.

[35] M. Bozzi, A. Georgiadis, et al. Review of Substrate-Integrated Waveguide Circuits and Antennas. *IET Microwaves, Antennas and Propagation*, 5(8):909–920, 2011.

[36] C.A. Balanis. *Antenna Theory*. Third edition, 2005.

[37] R. Bansal. *Fundamentals of Engineering Electromagnetics*. Taylor & Francis, 2006.

[38] J. van Bladel. On the Resonances of a Dielectric Resonator of Very High Permittivity. *IEEE Transactions on Microwave Theory and Techniques*, 23(2):199–208, February 1975.

[39] J. van Bladel. The Excitation of Dielectric Resonators of Very High Permittivity. *IEEE Transactions on Microwave Theory and Techniques*, 23(2):208–217, February 1975.

[40] R.K. Mongia and A. Ittipiboon. Theoretical and Experimental Investigations on Rectangular Dielectric Resonator Antennas. *IEEE Transactions on Antennas and Propagation*, 45(9):1348–1356, 1997.

[41] A. Rashidian and D.M. Klymyshyn. On the Two Segmented and High Aspect Ratio Rectangular Dielectric Resonator Antennas for Bandwidth Enhancement and Miniaturization. *IEEE Transactions on Antennas and Propagation*, 57(9):2775–2780, September 2009.

[42] W. Che, K. Deng, et al. Analytical Equivalence Between Substrate-Integrated Waveguide and Rectangular Waveguide. *IET Microwave Antennas Propagation*, pages 35 –41, 2008.

[43] P.L. Sulliwan and D.H. Schaubert. Analysis of an Aperture Coupled Microstrip Antenna. *IEEE Transactions on Antennas and Propagation*, 8(8):977–984, 1986.

[44] S.M. Shum and K.M. Luk. Analysis of an Aperture Coupled Rectangular Dielectric Resonator Antenna. *Electronics Letters*, 30(21):1726–1727, October 1994.